

JGR Oceans

RESEARCH ARTICLE

10.1029/2023JC020788

Special Collection:

The Arctic Ocean's changing Beaufort Gyre

Key Points:

- Autumnal Equinox pivotal in ocean surface energy budget: heat loss began to surpass solar radiation gain per shipboard and satellite data
- Post-equinox, synoptic turbulent heat flux variability surged, linked to frequent cold, dry air outbreaks with a duration of a few days
- Turbulent heat fluxes, five times longwave emission, accelerated ocean heat release, causing the Beaufort-Chukchi seas freeze in November

Correspondence to:

L. Yu, lyu@whoi.edu

Citation:

Carrigg, J., Yu, L., Menezes, V. V., & Chen, Y. (2024). Autumnal equinox shift in Arctic surface energy budget: Beaufort-Chukchi seas case study. *Journal of Geophysical Research: Oceans*, 129, e2023JC020788. https://doi.org/10.1029/2023JC020788

Received 6 DEC 2023 Accepted 9 MAY 2024

Author Contributions:

Conceptualization: Joseph Carrigg, Lisan Yu

Data curation: Lisan Yu, Viviane V. Menezes

Formal analysis: Joseph Carrigg, Lisan Yu, Viviane V. Menezes, Yanxu Chen

Funding acquisition: Lisan Yu, Viviane V. Menezes

Investigation: Joseph Carrigg, Lisan Yu, Yanxu Chen

Methodology: Lisan Yu, Viviane V. Menezes

Project administration: Lisan Yu, Viviane V. Menezes

Software: Lisan Yu, Yanxu Chen **Supervision:** Lisan Yu, Viviane V. Menezes

Validation: Joseph Carrigg, Lisan Yu, Viviane V. Menezes, Yanxu Chen Visualization: Lisan Yu Writing – original draft: Lisan Yu

© 2024. American Geophysical Union. All Rights Reserved.

Autumnal Equinox Shift in Arctic Surface Energy Budget: Beaufort-Chukchi Seas Case Study

Joseph Carrigg^{1,2}, Lisan Yu¹, Viviane V. Menezes¹, and Yanxu Chen¹

¹Department of Physical Oceanography, Woods Hole Oceanographic Institution, Woods Hole, MA, USA, ²College of Earth, Ocean, and Atmospheric Sciences, Oregon State University, Corvallis, OR, USA

Abstract This study examines the annual cycle of the Surface Energy Budget (SEB) in the Beaufort-Chukchi seas, focusing on the autumn transition. Shipboard measurements from NASA's Salinity and Stratification at the Sea Ice Edge (SASSIE) experiment (8 September–2 October 2022) and satellite flux analysis for the entire 2022 were utilized to provide a comprehensive perspective of the SEB's seasonal dynamics. An important finding is the alignment of SEB's autumnal transition with the September 22 equinox, marking the onset of prolonged Arctic darkness. This transition involved a shift from the summertime radiative heating to cooling conditions, characterized by outgoing longwave radiation surpassing incoming solar radiation and a notable increase in synoptic turbulent latent and sensible heat flux variability. The increased turbulent heat fluxes after the equinox were associated with increased occurrences of short-duration cold air outbreaks. These outbreaks seem to originate from cold mesoscale surface winds transitioning from cooling landmasses or ice caps to the warmer seas, driven by differential cooling rates between land/ice and ocean as solar irradiance declined. Turbulent heat losses, outpacing longwave emission by more than fivefold, accelerated ocean surface cooling in the subsequent 2 months, leading to the complete freeze-up of the Beaufort-Chukchi seas by late November. These findings underscore the substantial influence of astronomical seasons on the SEB, emphasizing their crucial role in Arctic climate dynamics.

Plain Language Summary This study is to enhance understanding of Arctic Surface Energy Budget (SEB) patterns, focusing on energy exchanges at the open sea surface over the year. It examines autumn energy transition in the Beaufort-Chukchi seas, using shipboard measurements from NASA's SASSIE experiment (8 September–2 October 2022) and satellite heat flux analyses for the entire year of 2022. These data sources offer insights into the energy flows and patterns in the region. An important finding is the alignment of the autumn energy transition with the September 22 equinox, marking the onset of the extended Arctic darkness and the transition from oceanic heat gain to loss. Cold air outbreaks from surrounding landmasses and ice caps increased, intensifying heat transfer from the ocean to the atmosphere through evaporation, conduction, and convection. Turbulent heat loss exceeded longwave emission by over fivefold, expediting ocean surface cooling over the subsequent 2 months, culminating in complete freezing of the Beaufort-Chukchi seas by late November. Understanding the influence of astronomical seasons on the SEB is crucial for comprehending and predicting the Arctic climate changes.

1. Introduction

The Arctic Ocean has pronounced annual variations in the surface energy budget (SEB). These variations result from intricate interactions among the atmosphere, ocean, and sea ice extent and are profoundly influenced by solar irradiance (Overland, 2009; Przybylak, 2016). During winter, limited sunlight results in continuous sea ice growth, while in summer, continuous daylight in the Arctic causes ice melt and ablation. The transitional seasons of spring and fall, coinciding with the vernal and autumnal equinoxes, are marked by noticeable changes in wind patterns, cloud formations, and air-sea-ice exchanges of heat and mass. The seasonal shifts in SEB, both influencing and influenced by the variations in ice albedos and the stratification of the upper ocean (Perovich & Polashenski, 2012; Uttal et al., 2002), are integral to the cyclical process of seasonal melting and freezing (Ricker et al., 2021; Stroeve et al., 2014; Timmermans, 2015). Given the Arctic's diverse trends, including rapid decline of sea ice volume (Comiso et al., 2008; Zhang, 2021), delayed autumn freezing (Stroeve et al., 2012), and a warming rate that is two to four times higher than the global average—termed Arctic amplification (Overland et al., 2019; Rantanen et al., 2022; Serreze & Barry, 2011; Steele & Dickinson, 2016)—understanding the processes that maintain the SEB is becoming ever more essential.

CARRIGG ET AL. 1 of 22



Journal of Geophysical Research: Oceans

10.1029/2023JC020788

Writing – review & editing: Joseph Carrigg, Lisan Yu, Viviane V. Menezes, Yanxu Chen The SEB includes key surface heat exchange processes such as incoming solar radiation, outgoing longwave radiation, turbulent latent heat flux from evaporation and sublimation, and sensible heat fluxes due to thermal conduction. However, direct observations of the SEB are limited. Our understanding of the Arctic SEB largely relies on atmospheric reanalysis, which assimilates historical observations with model dynamics to reconstruct past atmospheric states (Trenberth et al., 2001). The typical approach to estimating the Arctic SEB involves combining atmospheric model data with limited field observations within a "control volume" framework (Nakamura & Oort, 1988). In this approach, the Arctic is treated as a polar cap enclosed at 70°N, and the SEB is estimated as a residual, accounting for energy changes within the atmospheric column, the energy flux at the top of the atmosphere, and energy transport across the 70°N boundary. The same conceptual framework is also applied to the ocean, with boundaries set at the ocean surface or the top of sea ice, the ocean floor, and lateral land or sea passages. By using ocean temperature and salinity observations, this method allows for inferences of surface heat and freshwater budgets (Tsubouchi et al., 2018).

Annual SEB patterns in the Arctic, characterized by significant winter heat loss and substantial summer heat gain, are a consistent finding across all studies (Cullather & Bosilovich, 2012; Mayer et al., 2016; Nakamura & Oort, 1988; Overland, 2009; Porter et al., 2010; Serreze et al., 2007). Two unique aspects of this pattern stand out: the pronounced annual variations in solar insolation that is unparallel globally, and the relatively low moisture influence due to frigid conditions that limit the air's moisture-holding capacity (Andreas et al., 2002; Gettelman et al., 2006). In autumn, as the temperatures drop, the sensible heat flux can match or even exceed the latent heat flux in its impact on the SEB. This is a stark contrast to lower latitudes where latent heat flux typically dominates (Yu, 2019).

Although reanalysis-based SEB analysis offers valuable insights, accurate quantification of the annual SEB cycle and its seasonal transitions remains a challenge. The "control volume" method, which estimates the SEB as a residual, is prone to uncertainties from each component of the energy budget (Overland & Turet, 1994). Additionally, biases in atmospheric reanalysis can lead to significant discrepancies, thereby hindering a detailed quantitative assessment of the contribution of each process in maintaining the SEB and the balance of incoming solar radiation against other SEB components (Adams et al., 2000; Bromwich et al., 2010; Semmler et al., 2012; Serreze et al., 2007). As a result, crucial questions regarding the timing and mechanisms that govern the transition between heat gain and heat loss, as well as the specific atmospheric and oceanic conditions essential for sustaining the annual SEB cycle, are less clearly understood.

In-situ measurements, essential for capturing each component of the SEB and thus contributing to comprehensive SEB data sets, are crucial in addressing the knowledge gaps inherent in broader-scale, model-based studies. The task of conducting detailed surface energy exchange measurements becomes especially daunting in the Arctic Ocean, an environment plagued by unpredictable weather and often remote, nearly inaccessible locales. Consequently, data collected from the limited number of field programs operating in the Arctic region (e.g., Cohen et al., 2017; Inoue & Hori, 2011; Shupe et al., 2022; Uttal et al., 2002; Vüllers et al., 2020) hold immense value. Prominent among these field efforts are the Surface Heat Budget of the Arctic Ocean field experiment in the 1990s (Perovich et al., 1999; Uttal et al., 2002), and the more recent Multidisciplinary Drifting Observatory for the Study of Arctic Climate (MOSAiC) campaign, recognized as the most extensive Arctic drift campaign in the central Arctic to date (Cox et al., 2023; Shupe et al., 2022). Another significant recent initiative is NASA's Salinity and Stratification at the Sea Ice Edge (SASSIE) program (Drushka et al., 2024), conducted from 5th September to 2nd October 2022, in the Beaufort and Chukchi Seas (Figure 1). This program aimed to enhance our understanding of how salinity anomalies from summer ice melt affect the initiation of sea ice formation in early autumn. The field experiment amassed an extensive array of measurements using ship-based, aircraft-based, and autonomous platforms. Air-sea variables related to the SEB components were primarily obtained through shipboard instruments, with data sampling intervals as frequent as every 20 min.

The SASSIE data sets are invaluable not only as time-series benchmarks for evaluating satellite-based flux estimates but also possess significant scientific relevance due to the timing and location of the field program. Focused on September 2022, a pivotal month characterized by the lowest sea ice extent after the summer melt, these data sets offer unique insights into surface heat exchange during this transition period. The SASSIE ship navigated through the Beaufort-Chukchi seas, an area of considerable interest because of its rapid sea ice decline (Onarheim et al., 2018). Analyzing the SEB during September is essential to understand the influence of surface forcing on the processes that lead to the autumn ice formation.

CARRIGG ET AL. 2 of 22

21699291, 2024, 5, Downloaded from https://agupubs.onlinelibrary.wiley.com/doi/10.1029/2023/C020788 by Mbl Whoi Library, Wiley Online Library on [18/04/2025]. See the Terms

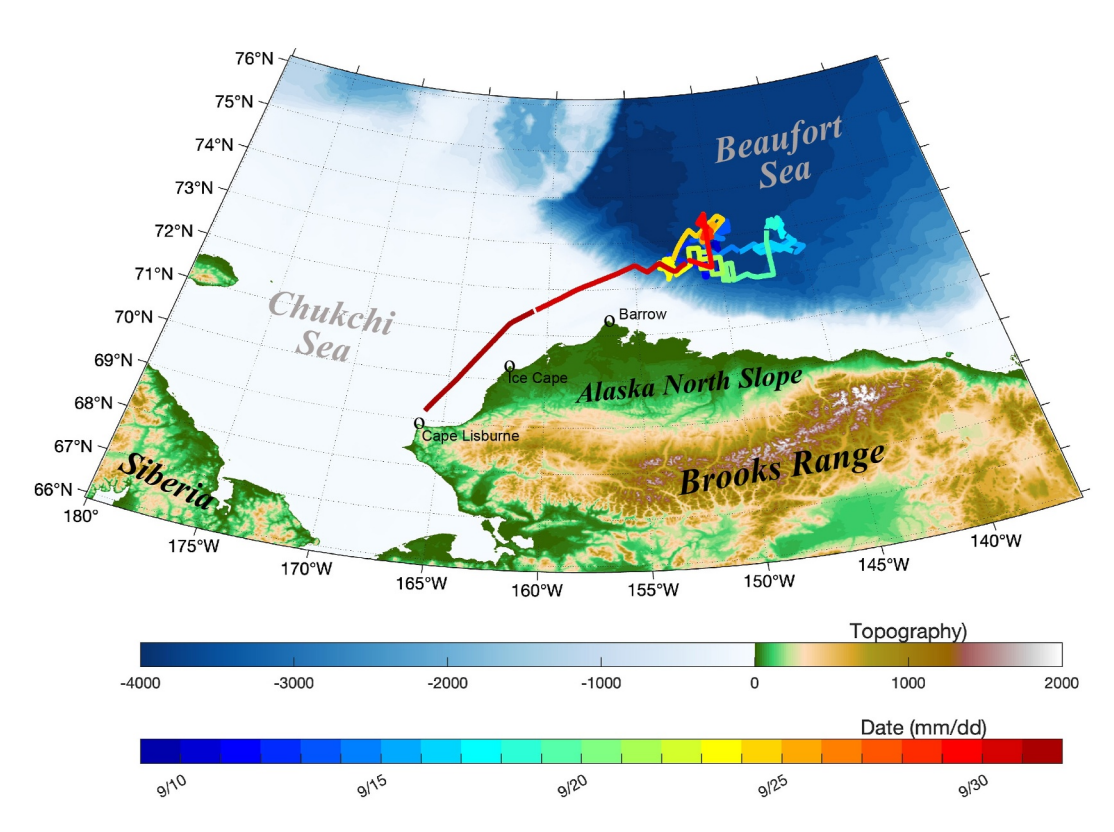


Figure 1. Topographical and bathymetrical map of the Beaufort and Chukchi seas region in the Arctic circle (66.5°N). The route taken by the Salinity and Stratification at the Sea Ice Edge field experiment ship from 8th September to 2nd October 2022, is superimposed and color-coded based on the date. Note that the shown ship route represents the dates when data were collected.

Additionally, the seasonal variations in the SEB of the Beaufort-Chukchi seas are closely tied to broader seasonal changes across the Arctic region. Figure 2 presents the monthly averaged distribution of the SEB in the Arctic ice-free regions for August, September, and October 2022. These monthly mean maps are derived from two satellite-based data sets. Surface short- and long-wave radiation data are obtained from the NASA Clouds and Earth's Radiant Energy Systems (CERES) Energy Balanced and Filled (EBAF) product (Loeb et al., 2018). Surface turbulent latent and sensible heat fluxes are sourced from the second-generation Objectively Analyzed air-sea Fluxes project (OAFlux2) (Yu, 2019; Yu & Weller, 2007). The transition in the SEB during these months is notable, with the SEB shifting from a net heat gain in August to a complete heat loss by October across the Arctic. September presents a mixed pattern, with modest heat gain and loss throughout the region. Importantly, the SEB changes within the Beaufort-Chukchi seas reflect broader Arctic energy transitions (e.g., Nakamura & Oort, 1988; Overland & Turet, 1994; Porter et al., 2010; Serreze et al., 2007), highlighting the significance of September as a key transitional period. Moreover, the Beaufort-Chukchi seas serves as an essential indicator for studying the complex energy dynamics of the Arctic.

This study examines the surface energy transition in the Beaufort-Chukchi seas during September 2022, focusing on the SASSIE shipboard data sets and satellite flux products from CERES and OAFlux2. It addresses two key issues: the interaction between surface radiation and turbulent heat fluxes that shapes the evolution of the SEB during this period of transition, and the interplay of these processes with the air-sea-ice conditions in the Beaufort-Chukchi seas, which is characterized by their seasonal sea ice cover over the ocean and bounded to the south by the Alaskan North Slope on land (Figure 1).

The data used for this study are described in Section 2. Analysis of shipboard measurements is presented in Section 3, and satellite insights on shipboard observed SEB changes and connection to the broader Beaufort-Chukchi seas are included in Section 4. Summary and conclusion are provided in Section 5.

CARRIGG ET AL. 3 of 22

21699291, 2024, 5, Downloaded from https://agupubs.onlinelibrary.wiley.com/doi/10.1029/2023JC020788 by Mbl Whoi Library, Wiley Online Library on [18/04/2025]. See the Terms

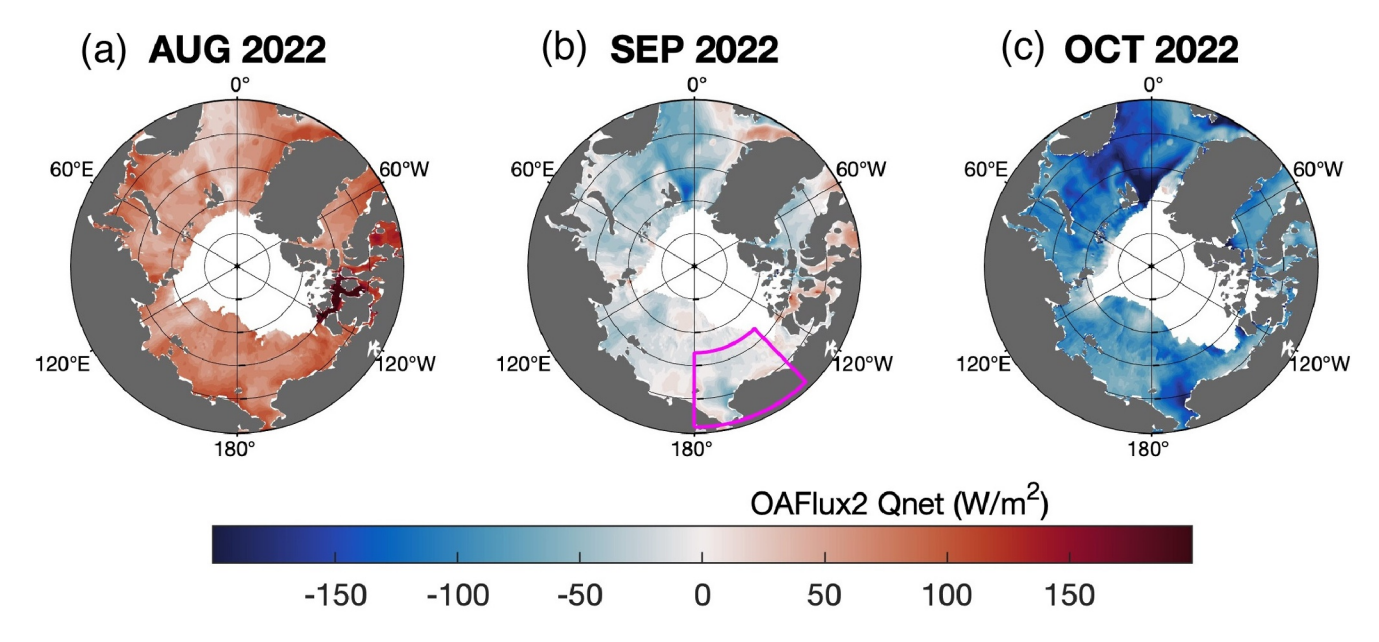


Figure 2. Net heat budget (Q_{NET}) at the Arctic Ocean Surface for (a) August 2022, (b) September 2022, and (c) October 2022. Positive values (red) indicate heat gain at the ocean surface, while negative values (blue) denote heat loss. The net heat budget, Q_{NET} , is the summation of surface shortwave, longwave, turbulent latent, and sensible heat fluxes, as sourced from the OAFlux2 project. In (b), the magenta-outlined area highlights the study region, which includes the scope of the Salinity and Stratification at the Sea Ice Edge field program (see Figure 1).

2. Data and Methods

2.1. SASSIE Field Experiment and the Study Domain

The SASSIE field experiment embarked from Homer, Alaska, aboard the research vessel R/V *Woldstad*. The vessel steered northward, heading toward the designated study area in the Beaufort Sea. On 8th September 2022, it arrived the marginal ice zone near 72°N, 150°W, marking the commencement of continuous shipboard air-sea measurements that lasted until 2nd October 2022 (Drushka et al., 2024). A chronology of the ship's movements and the time spent in each region is depicted in Figure 1, showing the ship's course through the Beaufort Sea, its transition across the Chukchi Sea, and the completion of its data collection near Cape Lisburne.

The study domain focuses on the Beaufort-Chukchi seas region, ranging from 180° to 135°W in longitude and from 66° to 76°N in latitude. This region encompasses the SASSIE ship course, providing a link between the localized air-sea conditions experienced by the ship and the broader basin-wide conditions. A detailed topographical and bathymetrical map of this domain is provided in Figure 1. Bathymetrically, the Beaufort Sea, where the SASSIE measurements began, features deeper waters compared to the shallower depths of the Chukchi Sea, where the data collection concluded. Geographically, the study area is bordered by the North Slope, north of the Brooks Range, to the south. The Brooks Range, a prominent mountain chain extending across the northern Alaska, acts as a significant geographical barrier that can influence meteorological and climatic patterns in the Beaufort-Chukchi seas (Overland, 2009; Zhang et al., 2018). High wind events frequently occur along the coast of the Alaskan North Slope, largely due to the complex orographic dynamics and seasonally varying surface conditions in the region (Kozo, 1980; Lynch et al., 2004; Stegall & Zhang, 2012).

2.2. Shipboard Air-Sea Measurements and Flux Calculation

2.2.1. Surface Flux Calculation

The net incoming shortwave radiation, Q_{SW} , is calculated as follows:

$$Q_{SW} = SW \downarrow (1 - \alpha) \tag{1}$$

where $SW\downarrow$ is incoming solar radiation, and α is surface albedo, which is typically set to the standard constant value of 0.055 (Fairall et al., 2003). For the purposes of this study, all fluxes are defined as positive when directed

CARRIGG ET AL. 4 of 22

downward and negative when directed upward, indicating the addition of heat to the ocean (a warming effect) for positive values and the release of heat from the ocean (a cooling effect) for negative values.

The calculation for net outgoing longwave radiation, Q_{LW} , uses the following formula:

$$Q_{LW} = \left(\varepsilon\sigma T_s^4 + \alpha_L LW\downarrow\right) - LW\downarrow \tag{2}$$

where $LW\downarrow$ is the measured downward facing longwave radiation, ε the effective emissivity of sea surface and set to be a constant 0.97, σ the Stefan-Boltzmann constant, 5.67 × 10⁻⁸ W m⁻² K⁻⁴, T_s the absolute sea surface temperature (SST) expressed in Kelvins (K), and α_L the surface longwave albedo and often set to 1 – ε in practice.

The calculation of turbulent sensible heat flux, Q_{SH} , and latent heat flux, Q_{LH} , is based on the bulk flux parameterization, expressed as follows:

$$Q_{SH} = \rho c_o c_h W \left(T_s - T_a \right) \tag{3}$$

$$Q_{LH} = \rho L_e c_e W \left(q_s(T_s) - q_a (RH) \right) \tag{4}$$

where ρ is air density, c_p the specific heat capacity of air at constant pressure, c_e and c_h are the turbulent exchange coefficients for sensible heat and latent heat, respectively, and L_e the latent heat of evaporation. The input variables are W for wind speed, T_a for air temperature, q_s for the sea-surface specific humidity, q_a for the air specific humidity that is calculated from relative humidity (RH). The Coupled Ocean-Atmosphere Response Experiment (COARE) algorithm version 3.5 (Edson et al., 2013) was used in computing Q_{SH} and Q_{LH} .

The SEB, denoted as Q_{NET} , is calculated by summing the radiative and turbulent heat fluxes as derived from Equations 1–4, as follows:

$$Q_{NET} = Q_{SW} - Q_{LW} - Q_{SH} - Q_{LH} (5)$$

2.2.2. Shipboard Measurements, Flux Calculation, and Uncertainty

The SASSIE vessel was equipped with a suite of surface meteorological instruments for comprehensive surface flux data collection. This included infrared and shortwave radiometers for measuring downward longwave and shortwave radiation, two air temperature sensors, two RH sensors, a barometric pressure sensor, two sonic anemometers recording wind speed and direction, and a Licor Li-7500 fast-water vapor sensor. These measurements were operational throughout the observation duration, from 8 September to 2 October 2022. The SASSIE shipboard surface meteorological observations and the calculated surface fluxes are available as 20-min averages and can be accessed from the JPL PO.DAAC (Menezes & Zippel, 2023). It is worth noting, however, that despite the installation of two RH sensors onboard, both encountered operational failures, resulting in no RH data being collected by the SASSIE field program. Also, due to operational issues, wind measurements from the anemometers are only available starting on 10 September. Hence, the data record for turbulent heat fluxes, and subsequently for Q_{NET} , encompasses a total duration of 26 days.

All air-sea variables necessary for the flux calculations in Equations 1–5 were obtained during the SASSIE observation period, with the exception for RH. Consequently, an assumption was made to estimate the shipboard Q_{LH} . Given the low Arctic temperatures, which limit the moisture-holding capacity of the air (Andreas et al., 2002; Gettelman et al., 2006), a constant RH of 89% was assumed for the duration of the observation. The Q_{LH} estimates derived from serve as the standard reference (Drushka et al., 2024). To assess potential uncertainties stemming from this assumption, two additional Q_{LH} calculations were conducted. The first calculation assumed drier atmospheric condition with an RH of 70%, which produced an upper bound for Q_{LH} (denoted as Q_{LH} —DRY). The second calculation assumed a fully saturated, wetter atmosphere with an RH of 100%. This led to a lower bound for Q_{LH} (denoted as Q_{LH} —WET). Thus, the range of uncertainty attributed to the RH assumption is defined by these two extreme values, Q_{LH} —WET and Q_{LH} —DRY.

To examine the impact of the uncertainty estimates on Q_{LH} , Figure 3a presents the 26-day time series of standard Q_{LH} values along with the uncertainty range defined by the upper (Q_{LH}_DRY) and lower (Q_{LH}_WET) bounds. Q_{LH} values are mainly negative, reflecting oceanic heat loss due to evaporation. During the 26-day measurement

CARRIGG ET AL. 5 of 22

com/doi/10.1029/2023JC020788 by Mbl Whoi Library, Wiley Onli

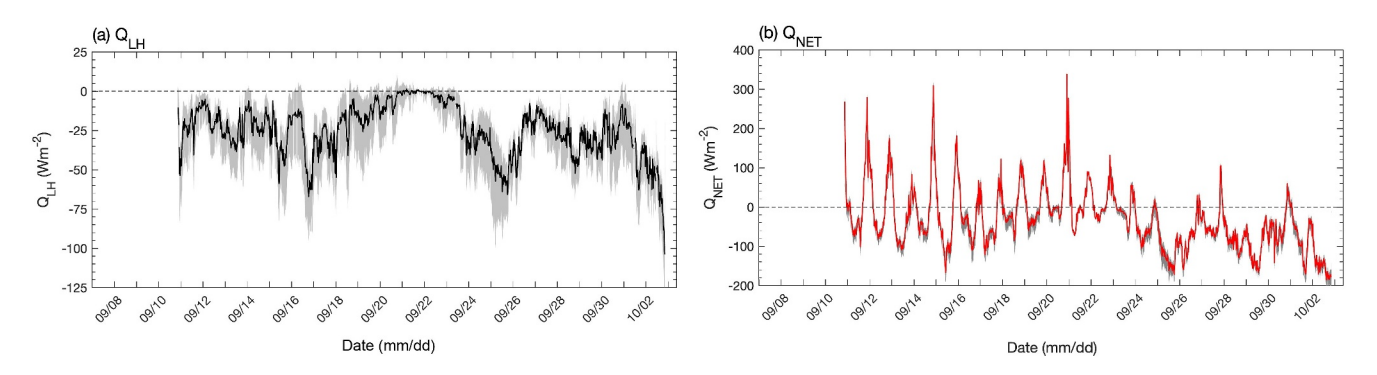


Figure 3. Uncertainty and effect of the Q_{LH} estimation due to relative humidity (RH) assumption. (a) Time series of 20-min standard Q_{LH} estimates with an RH set at 89% (black line). The gray shaded area denotes the uncertainty range bounded by Q_{LH} -WET (RH = 100%) and Q_{LH} -DRY (RH = 70%). (b) Time series of the 20-min shipboard surface heat budget estimates, Q_{NET} (red line), with the Q_{LH} uncertainty superimposed (gray shaded area).

period, the mean Q_{LH} was 25 Wm⁻² with a standard deviation (STD) of 16 Wm⁻². The mean uncertainty range, calculated as the difference between Q_{LH} wet and Q_{LH} and Q_{LH} and Q_{LH} aligning closely with the STD value of Q_{LH} . This alignment indicates that the uncertainty introduced by the RH assumption is comparable to the natural variability within the Q_{LH} estimates.

The uncertainty in Q_{LH} introduces uncertainty in Q_{NET} (Equation 5). In Figure 3b, the mean and STD of Q_{NET} were 32 and 75 Wm⁻², respectively. The uncertainty in Q_{NET} , calculated as 15 Wm⁻², represents about 20% of the STD of Q_{NET} . Given these values, the analysis of both Q_{LH} and Q_{NET} may need the uncertainty introduced by the RH assumption to ensure a reliable interpretation.

2.3. Satellite-Based Gridded Products

The satellite-based SEB for the Beaufort-Chukchi seas area is derived from two satellite flux analyses, the CERES EBAF surface radiation (Loeb et al., 2018) and OAFlux2 air-sea turbulent fluxes (Yu, 2019; Yu & Weller, 2007).

2.3.1. CERES EBAF Surface Radiation

This study utilizes daily 1° upward and downward shortwave and longwave surface radiation data from CERES synoptic (SYN) (Loeb et al., 2018). The daily CERES-SYN fluxes were derived through a combination of Moderate Resolution Imaging Spectroradiometer and geostationary satellite imagery (Doelling et al., 2013). These data were then used to produce the CERES EBAF-Surface fluxes, incorporating necessary corrections and adjustments to maintain consistency with CERES EBAF-TOA fluxes. For detailed information on the product, readers can refer to the study by Kato et al. (2018). The data sets used in this study focus on the year 2022 and daily net shortwave and longwave, Q_{SW} and Q_{LW} , were compiled.

2.3.2. OAFlux2 Surface Turbulent Fluxes

The surface heat fluxes, Q_{SH} and Q_{LH} , and surface winds from OAFlux2 are available at a 0.25° spatial resolution on daily basis (Yu, 2019; Yu & Weller, 2007). Wind data are derived by merging 19 satellite scatterometers and passive microwave radiometers and represents equivalent neutral wind at 10 m (Yu, 2021; Yu & Jin, 2014). Air temperature (T_a) and specific humidity (q_a) at 2 m are retrieved using satellite emissivity data from 13 microwave radiometers and sounders (Yu & Jin, 2018). T_s is taken from the Level 4 foundation SST produced by the Operational Sea Surface Temperature and Ice Analysis system (UK Met Office, 2005). Daily Q_{LH} and Q_{SH} fields are calculated from the COARE 3.5 algorithm (Edson et al., 2013; Fairall et al., 2003).

2.3.3. Sea Ice Cover

The daily Sea Ice Extent data from the National Snow and Ice Data Center (NSIDC) are utilized to determine the ice-covered areas within the satellite-derived surface flux data sets. OAFlux2 turbulent heat flux estimates are unavailable within 25 km of the ice edge or continental landmasses, a limitation owing to ice or land contamination in the emissivity retrievals from passive microwave radiometers. The SASSIE spent a substantial amount

CARRIGG ET AL. 6 of 22

of time either within or adjacent to the marginal ice zone in the Beaufort Sea until September 28 (Figure 1). On a few days during this period, OAFlux2 data were absent as the vessel was in proximity to the ice edge, falling within the aforementioned 25 km exclusion zone for reliable data collection. The NSIDC sea ice extent daily data set can be used to identify these grid points.

2.4. Satellite-Ship Data Alignment

To facilitate evaluation, satellite flux data need to be collocated with the SASSIE data along its route. This collocation process employed two distinct methods. The first involved aligning the two satellite data sets. CERES daily surface radiation data are provided at a 1° resolution, while the OAFlux2 daily turbulent heat fluxes are available at a finer 0.25° resolution. To ensure compatibility and integration, CERES data were linearly interpolated to match the OAFlux2 grids. Following this interpolation, the CERES data sets were combined with the OAFlux2 data to produce Q_{NET} fields.

The second method involved collocating satellite data to the ship route. Shipboard measurements were provided at 20-min intervals along an irregular course. For the purpose of comparison with satellite data, a 3-hr evaluation window was chosen. This window aligned with the minimal sampling intervals that could be collectively supported by the various sensors contributing to the satellite products. The shipboard data were segmented into 3-hr blocks, ending at intervals such as 3, 6, and so forth. Satellite data were linearly interpolated to fit these 3-hr windows, with the daily average corresponding to the window concluding at 12. The interpolated satellite data were then mapped to the ship locations utilizing the inverse distance weighting method (Shepard et al., 1968).

2.5. Statistical Analysis

Linear regression is applied to analyze the variation of solar radiation associated with seasonal progression and the resultant downward flux in daily Q_{NET} changes. This analysis involved fitting a linear regression model to the data and calculating the coefficients of determination.

3. Shipboard Surface Heat Budget Analysis

3.1. Surface Heat Flux Variability in September

The time series of surface flux components and net heat flux budget, based on the SASSIE measurements taken at 20-min sampling intervals, are presented in Figures 4a–4e. Positive heat flux values denote heat flux directed downward, indicating oceanic heat gain, while negative values indicate heat flux directed upward, representing oceanic heat loss. The observed $SW\downarrow$ and $LW\downarrow$ (Figure 4a) are particularly insightful. Diurnal variations in $SW\downarrow$ are evident, with daily peaks corresponding to daylight hours. A clear progressive reduction in the amplitude of these diurnal peaks was observed. In early September, peaks were slightly above $400 \, \mathrm{Wm}^{-2}$, but they decreased to below $100 \, \mathrm{Wm}^{-2}$ by the end of the month. This reduction is consistent with the seasonal reduction in solar declination and the resultant shortening of daylight duration (Nakamura & Oort, 1988).

In contrast, the magnitude of $LW\downarrow$ remained relatively stable throughout the observation period. This stability suggests a continual emission of thermal infrared radiation from the atmosphere, which appears largely unaffected by the diurnal or seasonal changes observed in $SW\downarrow$. The distinct behaviors of $SW\downarrow$ and $LW\downarrow$ highlight the different dynamics and drivers behind these two key components of the surface radiative energy budget.

The time series of Q_{LH} and Q_{SH} (Figure 4b) show that these fluxes are predominantly negative, with occasional peaks exceeding $-75~{\rm Wm}^{-2}$, indicating the transfer of heat from the ocean to the atmosphere through turbulent motions. Notably, both fluxes display similar magnitudes, a characteristic commonly observed in polar seas (Andreas et al., 2002; Gettelman et al., 2006; Nakamura & Oort, 1988; Yu et al., 2019). In the cold conditions prevalent in the study area, the air's limited moisture-holding capacity diminishes the energy required for water's phase transition from liquid to vapor, thereby decreasing Q_{LH} values. Concurrently, the significant temperature differences between the relatively warmer ocean surface and cooler Arctic air facilitates a robust heat transfer to the atmosphere, evidenced by increased Q_{SH} values.

The net surface radiation, calculated as $Q_{SW} - Q_{LW}$ and shown in Figure 4c, depicts the net incoming solar radiation after accounting for the effects of net outgoing Q_{LW} . Strong diurnal variations are featured, with periods of net radiative heat gain (positive values) during daylight hours and net radiative heat loss (negative values) at night.

CARRIGG ET AL. 7 of 22

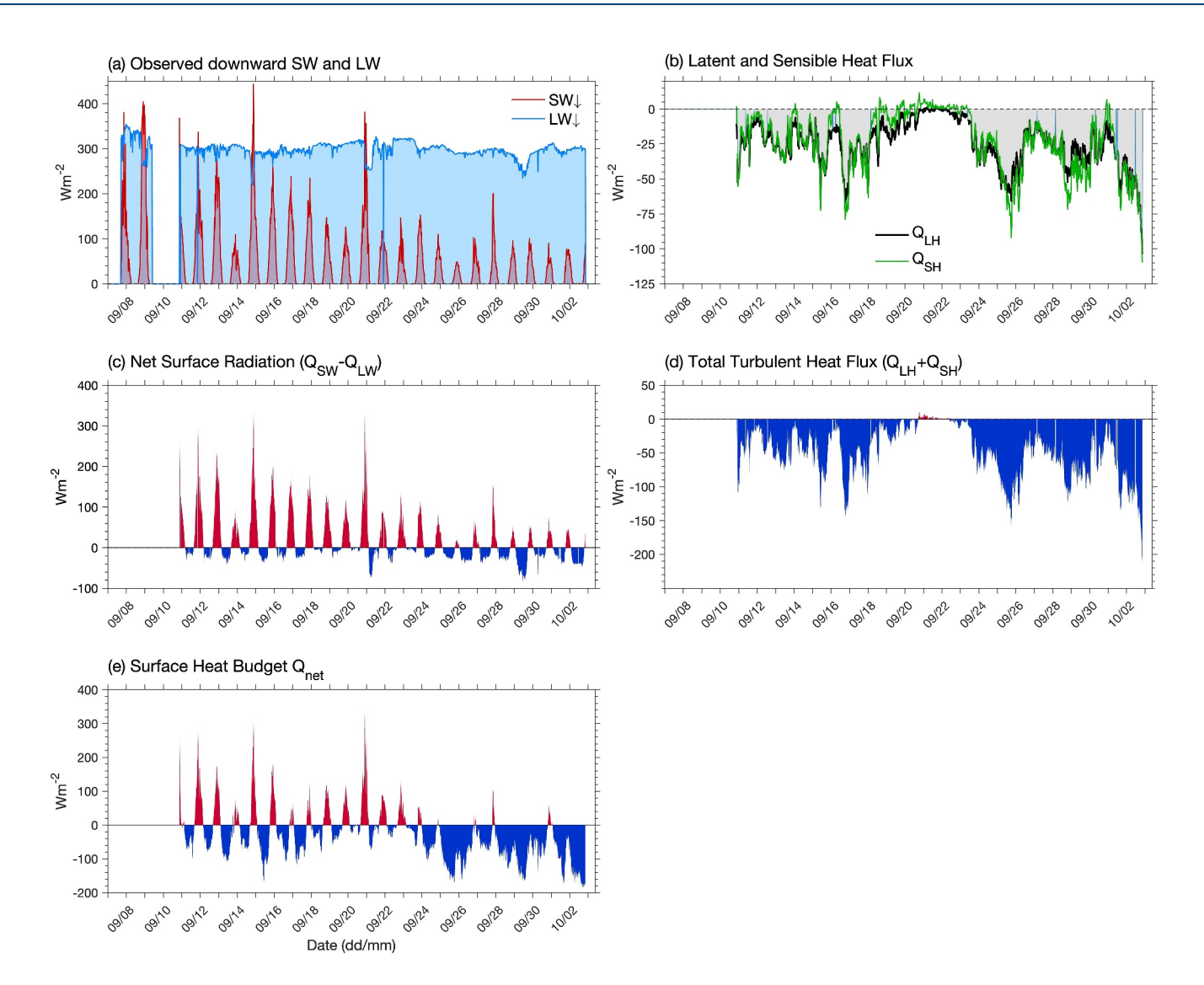


Figure 4. Time series of surface flux components and net fluxes based on Salinity and Stratification at the Sea Ice Edge measurements at 20-min intervals for the period of 8th September–2nd October 2022. (a) Measured downward shortwave ($SW\downarrow$; red shading) versus longwave radiation ($LW\downarrow$; blue shading), (b) Latent heat flux (Q_{LH} ; gray shading) vs. sensible heat flux (Q_{SH} ; green line), (c) Net surface radiation ($Q_{SW} - Q_{LW}$), (d) Total turbulent heat flux ($Q_{LH} + Q_{SH}$), and (e) Surface heat budget Q_{NET} . The fluxes, Q_{SW} , Q_{LW} , Q_{LH} , Q_{SH} , and Q_{NET} are estimated from Equations 1–5 using shipboard measurements. Positive (negative) value denotes heat flux directed downward (upward), indicating an oceanic heat gain (loss).

There was a noticeable gradual decrease in net radiative gain over the 26-day observing period. This pattern aligned with the seasonal progression toward lower solar irradiance. The range of net radiation varied broadly, with values dipping as low as -80 Wm^{-2} during the night to reaching peaks of 300 Wm⁻² during the day.

The total turbulent heat flux, summed as $Q_{LH} + Q_{SH}$ and represented in Figure 4d, was predominantly negative for the duration of the observation. However, there was a brief period during 20–22 September, during which the turbulent heat flux showed slightly positive values or hovered near zero. After this short interval, turbulent heat loss was evidently stronger, possibly reflecting strengthening air-sea temperature gradients with the advance of the season. The range of the total turbulent heat flux varied significantly, extending from as low as $-150 \,\mathrm{Wm}^{-2}$ to occasionally just a few Wm^{-2} above zero.

The SEB, represented by Q_{NET} in Figure 4e, reflects the balance between radiative and turbulent heat fluxes. This balance underwent two distinct phases. Initially, the daily heat budget was primarily driven by diurnal patterns, characterized by solar heat gains during daylight hours being compensated by losses at night. As the season advanced, however, a clear shift occurred toward a regime characterized by consistent net heat loss. This

CARRIGG ET AL. 8 of 22

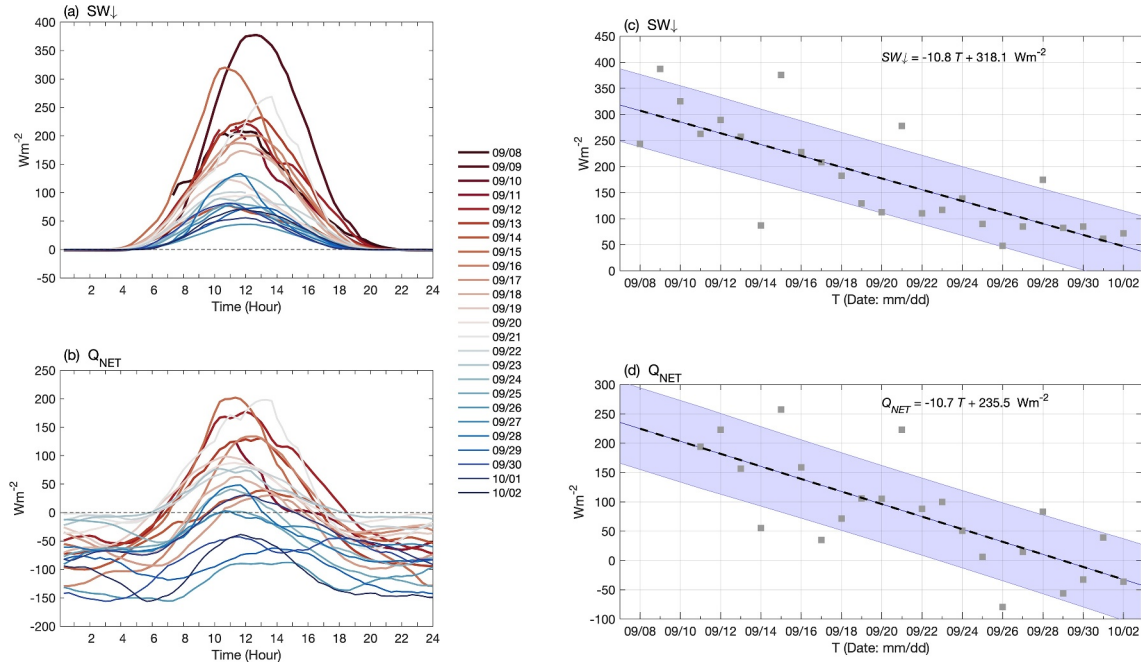


Figure 5. Diurnal variations of (a) $SW\downarrow$ and (b) Q_{NET} in local time (UTC-10). Each curve is color-coded according to date. A 4-hr (11-point running) mean is applied to the 20-min sampled time series. Linear regression of daily maxima of (c) $SW\downarrow$ and (d) Q_{NET} . The gray dots denote the daily maxima, and the linear regression is represented by a dashed line, with the calculated slope and intercept listed on the panel. The purple shaded area represents the 95% prediction interval for the regression.

transition from a cycle primarily driven by diurnal variations to one predominantly influenced by heat loss processes is significant, underscoring the increasing impact of heat loss processes as solar heat input diminishes.

However, the regime shift is not solely due to longwave heat loss (Figure 4c). The substantial role played by turbulent heat loss (Figure 4d) is equally important. The intensified turbulent heat loss emerged as a key player in this dynamic, significantly contributing to the marked transition in the surface heat exchanges observed in the Beaufort-Chukchi seas during September.

3.2. Reduction in Daily Maximum of $SW\downarrow$ and Q_{NET}

Figure 5a, presented in local time (UTC-10), shows the variations in the diurnal pattern of downward shortwave radiation ($SW\downarrow$) over the 26-day observation period. Each line in the graph is color-coded according to date. To minimize the impact of short-term fluctuations, a 4-hr (11-point) running mean was applied to the time series sampled at 20-min intervals. There was a marked decline in the peak values of $SW\downarrow$, dropping from almost 400 Wm^{-2} at the start of the vessel in early September to around 50 Wm^{-2} by the end of the month. The change aligned with the seasonal decrease in daylight hours and solar zenith angle as autumn set in.

As shown in Figure 4e, the diurnal variations of $SW\downarrow$ was the primary driver of daily fluctuations in Q_{NET} . To assess the impact of the reduction in $SW\downarrow$ on Q_{NET} , the diurnal patterns of Q_{NET} were also complied for the same 26-day period (Figure 5b). This compilation revealed a consistent decline in the maximum daily values of Q_{NET} , consistent with the decrease observed in $SW\downarrow$. Initially, peak values of Q_{NET} were around 200 Wm⁻², but during the observation period, these values progressively dipped down to about -100 Wm^{-2} . Particularly notable was the significant reduction in the diurnal range toward the latter part of September, with daily maximum Q_{NET} values transitioning into negative regime.

To quantify the daily decrease in $SW\downarrow$, a regression analysis was conducted on the daily $SW\downarrow$ maxima. The analysis, shown in Figure 5c, aimed to calculate the rate of reduction over the observation period. In the scatter plot, each data point corresponds to the maximum $SW\downarrow$ for a given day. The resulting trend line displays a negative slope, suggesting an average daily decrease of 10.8 Wm⁻² in incoming solar radiation at the sea surface during the observation period.

CARRIGG ET AL. 9 of 22

from https://agupubs.onlinelibrary.wiley.com/doi/10.1029/2023JC020788 by Mbl Whoi Library, Wiley Online Library on [18/04/2025]. See

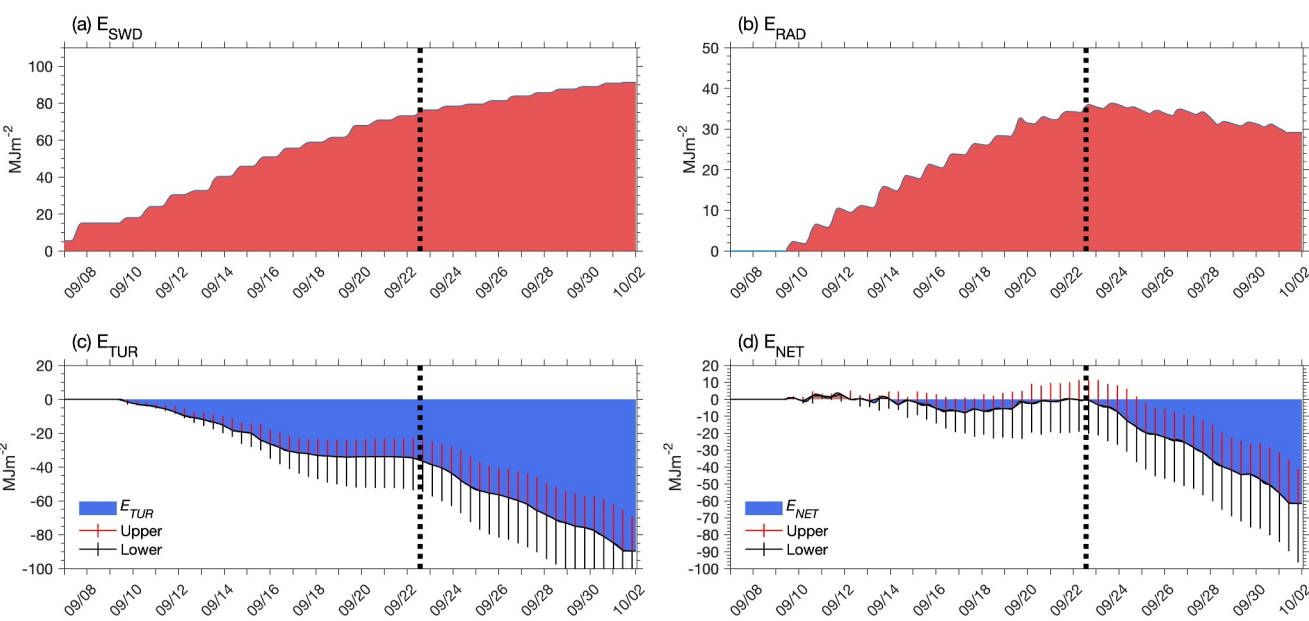


Figure 6. Change in heat energy transfer (measured in MJ m⁻²) during the Salinity and Stratification at the Sea Ice Edge 26-day observing period. (a) Downward solar radiation E_{SWD} , (b) net radiative heat energy E_{RAD} , (c) turbulent heat energy E_{TUR} , and (d) net heat energy E_{NET} . Positive values indicate heat received at the ocean surface, while negative values represent ocean heat loss to the atmosphere. In (c) and (d), the E values calculated from the standard references, E_{TUR} and E_{NET} , are shown, along with the uncertainty range defined by the lower- and upper- bound estimates, corresponding to Q_{LH} _DRY (RH = 70%) and Q_{LH} _WET (RH = 100%) approximations, respectively. The vertical thick dashed line marks the autumnal equinox on 22 September 2022.

A similar regression analysis was conducted on the daily Q_{NET} maxima (Figure 5d). This analysis revealed a comparable downward trend, with an average daily decline of 10.7 Wm⁻² in Q_{NET} . The close similarity in the rates of reduction between Q_{NET} and $SW\downarrow$ underscores the significance of $SW\downarrow$ as the primary driver of the SEB transition during September.

3.3. Surface Heat Energy Budget Transition at Autumnal Equinox

The cumulative heat energy, denoted as *E*, resulting from the air-sea heat exchange along the SASSIE route, can be quantified using the following integral equation:

$$E = \int Qdt \tag{6}$$

where the integral spans the entire 26-day observation period, with dt representing the 20-min sampling intervals. E is quantified in units of MJ m⁻² (10⁶ J m⁻²). Equation 6 was applied to four different sets of fluxes, $SW\downarrow$, $Q_{SW}-Q_{LW}, Q_{LH}+Q_{SH}$, and Q_{NET} . These calculations enable the quantification of energy transfer due to downward shortwave radiation (denoted as E_{SWD}), the net radiative flux (denoted as E_{RAD}), the total turbulent heat fluxes (denoted as E_{TUR}), and the overall SEB (denoted as E_{NET}), as shown in Figures 6a-6d.

The E_{SWD} values through the observation period (Figure 6a) show a continuous buildup of thermal energy in the ocean through solar radiation, emphasizing $SW\downarrow$ as the primary heat source for the Arctic Ocean from summer into fall. In contrast, the E_{RAD} pattern (Figure 6b) deviates from that of E_{SWD} . Following an initial increase, E_{RAD} reached its peak on September 22—the date of the autumnal equinox—before undergoing a marked decline. This date is pivotal as it marks the Earth's axis tilting away from the Sun, which leads to reduced daylight, a lower solar zenith angle, and subsequently, diminished solar radiation. The equinox, a period characterized by the sun's rapidly decreasing declination, sees a precipitous drop in solar radiation.

Following the equinox, E_{RAD} shows a distinct shift, indicating a transition at the ocean's surface from absorbing solar radiation to emitting radiative heat into the atmosphere. Hence, despite the continued increase in E_{SWD} , the increased emission of longwave radiation started to outweigh the heat gain from solar radiation. This reversal in

CARRIGG ET AL. 10 of 22

21699291, 2024, 5, Downloaded from https://agupubs.onlinelibrary.wiley.com/doi/10.1029/2023JC020788 by Mbl Whoi Library. Wiley Online Library on [1804/2025]. See

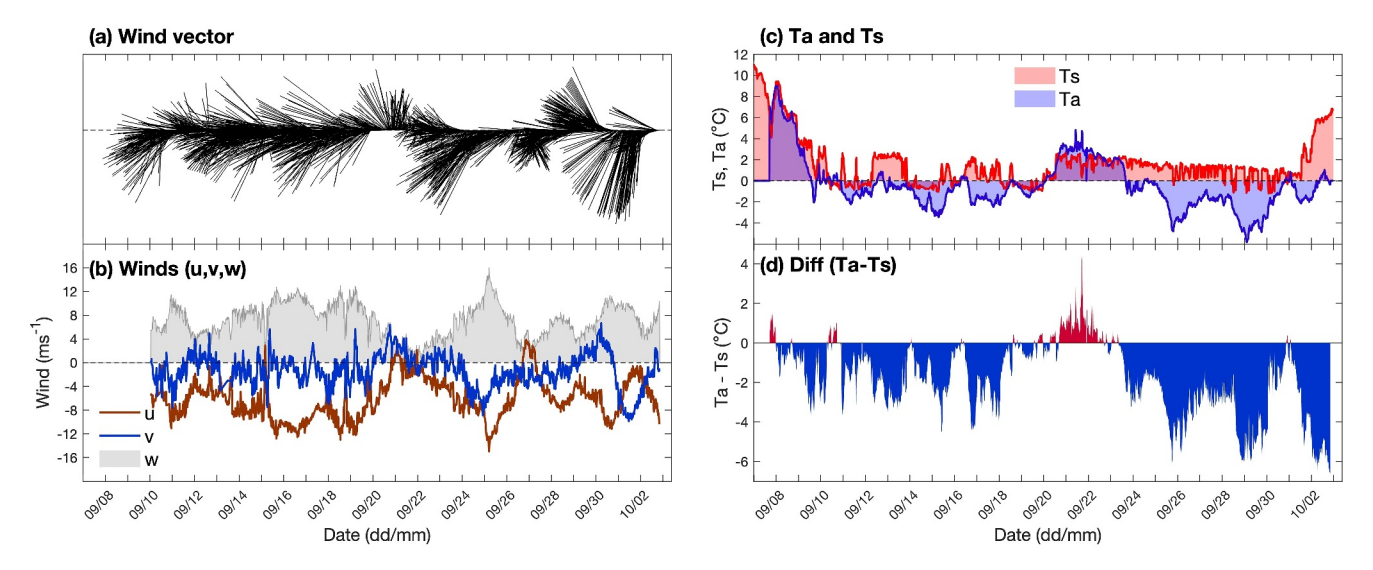


Figure 7. Time series of (a) wind vector (sticks) and (b) zonal (u; red line), meridional (v; blue line), and wind speed (w; gray shading and outline). In (a) the wind vector represents the direction from which the wind is blowing, with southeasterly winds mostly above the horizontal dashed line and northeasterly winds below it. Panels (c) and (d) display time series of air temperature (T_a ; blue shading and outline) and sea surface temperature (T_s ; red shading and outline), along with air-sea temperature differences ($T_a - T_s$; positive in red shading and negative in blue shading).

the surface net radiative energy exchange at the ocean surface highlights the significant astronomical impact on the seasonal thermal energy changes in the Arctic.

A significant turning point is also evident in E_{TUR} (Figure 6c), which represents the cumulative buildup of turbulent heat loss (indicated by negative values) from the ocean to the atmosphere. The figure includes blue and red error bars, corresponding to the uncertainties in E_{TUR} values arising from Q_{LH} _DRY and Q_{LH} _WET scenarios, respectively. The E_{TUR} estimates from Q_{LH} _DRY imply a greater heat loss compared to those from Q_{LH} _WET. Notably, on September 22 at the autumnal equinox, coinciding with the Earth's axial tilt away from the Sun, a marked intensification in turbulent heat loss is apparent across all E_{TUR} trends, regardless of the RH assumptions. This shift indicates an increased heat transfer of radiative heat accumulated in the ocean to the atmosphere, a change that occurred in synchrony with the astronomical seasonal transition.

The overall SEB, E_{NET} (Figure 6d), reveals a distinct pattern: leading up to the autumnal equinox from September 8–21, the radiative heat gain E_{RAD} and turbulent heat loss E_{TUR} almost balanced each other out, resulting in a near-zero net heat accumulation for this period. Post the equinox, however, E_{NET} entered a phase of steady decline. The E_{NET} estimates from $Q_{LH}DRY$ and $Q_{LH}WET$, represented by the respective black and red error bars, display similar patterns, though the values prior to the Autumnal equinox were slightly more negative for the former and more positive for the latter.

Despite uncertainties in E_{NET} due to the RH assumptions, the Autumnal equinox had a profound impact on surface energy dynamics, leading to a significant shift in the energy transfer patterns (Figures 6a–6d). The influence of the equinox reverberates through all energy terms, affecting both the radiative flux entering the ocean and the turbulent thermal outflow into the atmosphere. This marked change in the SEB at the time of equinox highlights the essential role of this astronomical event in shaping the seasonal rhythms and fundamental processes within the Arctic climatic system.

3.4. Shift in Wind Direction at the Equinox

Figure 6 brings to light an intriguing question about what triggered the intensification of turbulent heat fluxes to coincide with the Autumnal equinox. Unlike surface radiation fluxes that are directly influenced by solar insolation, turbulent heat fluxes are primarily driven by wind patterns and the temperature and humidity gradients between the sea surface and the overlying air (see Equations 3 and 4). To understand the mechanism behind this shift, an analysis was conducted focusing on changes in wind patterns and air and sea temperatures (Figures 7a–7d). Unfortunately, since humidity measurements were unavailable, we did not analyze latent heat fluxes.

CARRIGG ET AL. 11 of 22

In Figure 7a, the wind vector (represented by the sticks) indicates the direction from which the wind is blowing. Before the September 22, the dominant wind patterns were primarily easterly to northeasterly, with occasional southeasterly intervals. After September 22, a noticeable shift occurred, characterized by an increase in northeasterly winds and a reduction in southeasterly winds. This change in wind direction is further corroborated by the zonal (u) and meridional (v) wind component time series (Figure 7b). After this date, meridional wind variability became more substantial, while the influence of zonal winds showed a slight weakening. Interestingly, this shift in wind direction was not accompanied by an increase in wind speed.

Surface air temperatures, T_a , showed a noticeable decrease after September 22 (Figure 7c). This decline was marked by two distinct episodes of cold air. The first episode, occurring around September 26, was closely associated with a significant northeasterly wind event, while the second, taking place a few days later on September 29, was linked to a substantial southeasterly event. During both episodes, air temperatures fell below -5° C. Prior to September 22, there were a few occurrences of cold bursts, but these only brought the air temperature down to around -2 to -3° C.

Conversely, sea surface temperatures, T_s , tended to be colder before September 22 compared to after. This pattern is related to the SASSIE vessel's location, as the ship spent a substantial amount of time either within or near the marginal ice zone in the Beaufort Sea until 28 September (see Figure 1). As a result, T_s was higher whenever the vessel was not in close proximity to the ice. The initial cold northeasterly event appears to have occurred near the ice in the Beaufort Sea, while the subsequent cold southeasterly event unfolded in the open Beaufort-Chukchi seas. Nonetheless, the synoptic variability in T_s was not as marked as that in T_a , leading to the variability of $T_a - T_s$ being predominately influenced by T_a (Figure 7d).

The linewise observations from the ship do not provide specific details on the origins of these synoptic occurrences. However, the observed characteristics are consistent with cold air outbreaks typically originating from the continental landmasses or ice-covered areas, as documented in previous studies (Businger, 1987; Fletcher et al., 2016; Fore et al., 2012; Pichugin et al., 2019). These occurrences are commonly observed around the Autumnal equinox, a time when reduced solar radiation leads to more rapidly cooling of both land and ice-covered regions compared to the ocean, largely due to the ocean's greater heat capacity. This differential cooling results in the formation of localized pressure gradients, which subsequently drive mesoscale winds along these gradients (Lynch et al., 2004; Stegall & Zhang, 2012). Therefore, it is plausible that the varying thermal responses of air, land, and ocean to diminishing solar radiation plays a crucial role in intensifying turbulent heat fluxes coinciding with the arrival of the Autumnal equinox.

3.5. Cold Air Outbreaks and Enhanced Turbulent Heat Fluxes

The analysis in Figures 7a–7d indicates that changes in air temperatures were more pronounced than changes in wind speed during the cold air outbreaks. To assess their individual impacts on the changes in Q_{SH} , Equation 3 was decomposed into mean and anomalous components (Cayan, 1992) and reformulated as follows:

$$Q'_{SH} = \rho_a c_p c_h \left(\overline{W} \Delta T' + W' \overline{\Delta T} + W' \Delta T' \right) \tag{7}$$

where the overbars denote the time mean over the 26-day observation period and primes are 20-min deviations from the mean. If the effect of c_h is not considered, the three terms inside the brackets can be represented as follows: Tterm for $\overline{W}\Delta T'$, Wterm for $W'\overline{\Delta T}$, and Cterm for $W'\Delta T'$. These terms correspond to the contributions of thermal, wind, and nonlinear covariance effects on the total variability $(W\Delta T)'$, denoted as SHterm. Time series of these terms are shown in Figure 8.

The relative contribution of each term to SH term, determined by variance contribution (Γ), is calculated as follows (Yu et al., 2023):

$$\Gamma = \frac{\text{cov(term, SHterm)}}{\text{var(SHterm)}} \times 100\%$$
 (8)

Here, Γ can be considered as the proportion of variance in Q'_{SH} attributable to the respective effect in Equation 7.

CARRIGG ET AL. 12 of 22

21699291, 2024, 5, Downloaded from https://agupubs.onlinelibrary.wiley.com/doi/10.1029/2023JC020788 by Mbl Whoi Library, Wiley Online Library on [18/04/2025]. See the Terms

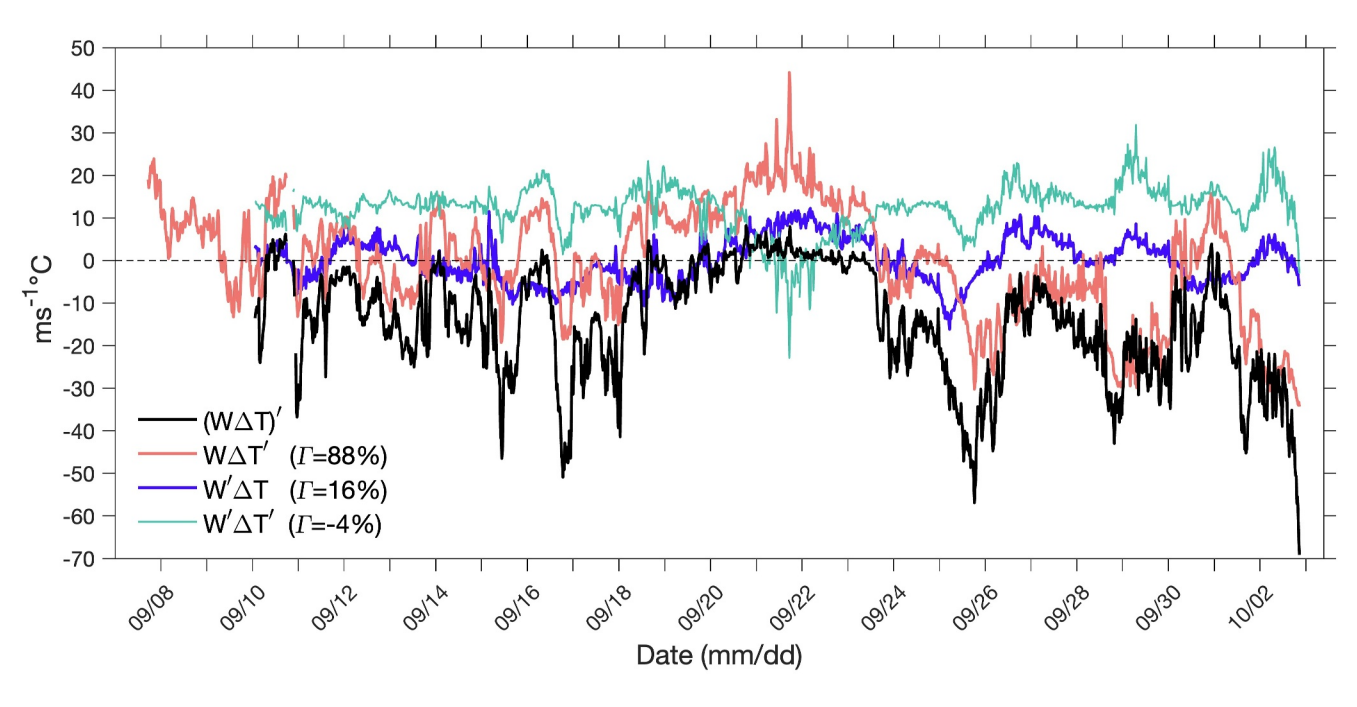


Figure 8. Relative contribution of three effects to the total variability SHterm ($(W\Delta T)'$; black line): Term ($\overline{W}\Delta T'$; red line) Wterm ($W'\overline{\Delta T}$; purple line) and Cterm ($W'\Delta T'$; green line). Γ measures the percentage of contribution of each term to the SHterm variance. A positive value of Γ indicates a positive contribution, while a negative value suggests a counteractive effect.

Figure 8 reveals that the Tterm (red line) is the predominant contributor influencing the variance of SHterm, accounting for 88% of its variability. Specifically, the enhanced SHterm during the two cold air outbreaks post the Autumnal equinox were mainly driven by the enhanced sea-air temperature contrast. By comparison, the Wterm (purple line) has a lesser impact, contributing to only 16% of the SHterm variance. The Cterm (green line) has a slight negative effect, representing a—4% contribution. The negative value indicates that the interactions between temperature and wind speed variations slightly counteract the overall variability of SHterm. These Γ values show that the variability of SHterm is predominantly dictated by the sea-air temperature variability (Tterm), with wind speed (Wterm) having a smaller and sometimes inverse relationship to SHterm variability.

The analysis of thermal and wind effects on Q_{SH} highlights the direct role of sea-air thermal variability in intensifying turbulent heat loss from the ocean after the Autumnal equinox. Concurrently, wind played an essential but indirect role in this process. The increase in sea-air temperature gradient, as seen in Figure 7, was largely due to changes in wind direction, which brought the influx of cold air masses from continents or perennial sea ice cover. In such events, sea-air temperature differences reached as much as -6° C, even though wind speeds did not experience significant increase.

Arctic cold air outbreaks are frequently associated with polar lows (Businger, 1987; Emanuel & Rotunno, 1989), which are short-lived yet intense cyclones typically lasting 1–2 days (Stoll et al., 2018). Inoue and Hori (2011) documented an instance of explosive frontal cyclogenesis at the marginal ice zone in the Beaufort-Chukchi seas during 23–27 September 2010. Using shipboard measurements from Doppler radar and radiosonde instruments aboard the Japanese R/V *Mirai*, they showed that dry and cold air masses, upon reaching the ocean, rapidly acquired heat and moisture from the warmer sea. This interaction had a significant impact on the marine boundary layer and cloud formation (Liu et al., 2004). Although confined to near-surface observations, the SASSIE meteorological measurements effectively demonstrated the enhancement of turbulent heat fluxes during synoptical weather conditions following the Autumnal equinox.

4. Satellite Insights on September Surface Energy Transition

The analysis of shipboard measurements has offered valuable insights into the surface energy transition in September, highlighting several key aspects:

CARRIGG ET AL. 13 of 22

21699291, 2024, 5, Downloaded from https://agupubs.onlinelibrary.wiley.com/doi/10.1029/2023/C020788 by Mbl Whoi Library, Wiley Online Library on [18/04/2025]. See the Terms

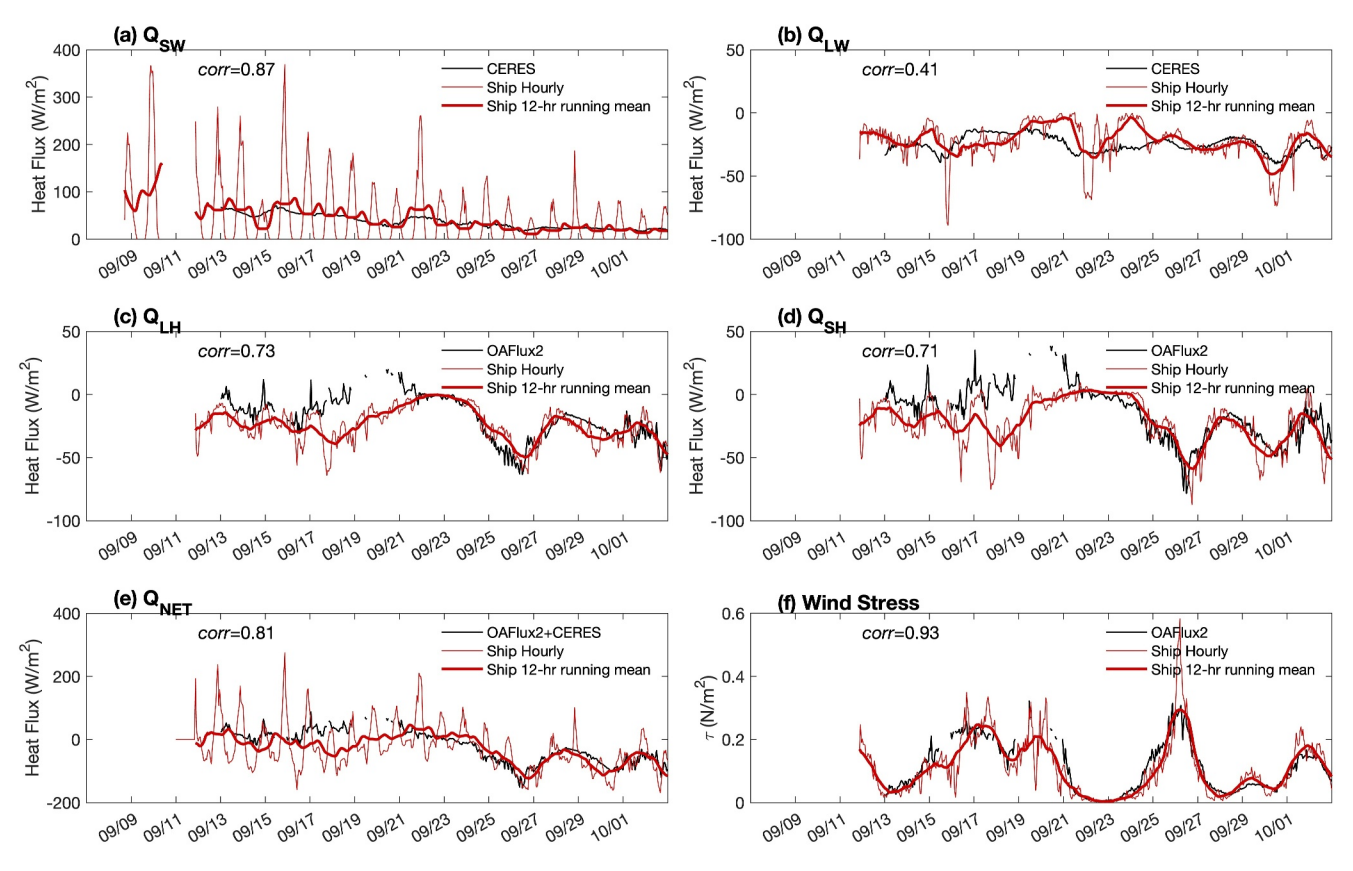


Figure 9. Comparison of satellite fluxes with shipboard flux estimates along the ship route for (a) Q_{SW} , (b) Q_{LW} , (c) Q_{LH} , (d) Q_{SH} , (e) Q_{NET} , and (f) τ . The 20-min shipbased fluxes (thin red line) were smoothed using 12-hr running mean (thick red line) to facilitate the comparison with 3-hourly interpolated satellite fluxes with daily resolution (black line). The correlation coefficient for each satellite-ship pair is listed on the panel.

- The transition in surface heat energy aligned precisely with the Autumnal equinox, marking a shift from ocean absorbing heat to releasing it.
- The influence of the equinox extended beyond altering net radiative flux into the ocean, also significantly
 enhancing ocean turbulent heat transfer to the atmosphere.
- Synoptic weather events, likely influenced by interactions among land, ice, air, and ocean, were instrumental in increasing turbulent heat exchange post-equinox.

However, these shipboard measurements were specific to a route through the southern Beaufort Sea and along the coastlines of the Alaska North Slope in the Chukchi sea (Figure 1). To fully understand the scope of these linewise findings and their relevance to the broader changes across the Beaufort-Chukchi seas, a more comprehensive assessment is required. Thus, satellite flux data are examined here to evaluate and broaden the insight derived from the shipboard data.

4.1. Satellite Flux Analysis Along the Ship Route

To ensure consistency between satellite and shipboard flux estimates, a comparison was conducted along the ship route for all flux components. As described in Section 2, satellite Q_{SW} and Q_{LW} are taken from CERES EBAF (Loeb et al., 2018), while satellite Q_{LH} and Q_{SH} , as well as wind stress, τ , are from OAFlux2 (Yu & Weller, 2007). Q_{NET} is the combination of the two products. The daily satellite products were interpolated to 3-hr intervals along the ship route. The time series of satellite fluxes versus shipboard flux estimates at 3-hr intervals are presented in Figures 9a–9f.

Two key considerations are crucial in this satellite-ship comparison. First, the daily satellite products cannot capture the diurnal variations that are a hallmark of shipboard measurements. Moreover, satellites provide area-averaged values of instantaneous measurements across their spatial footprints, in contrast to the point

CARRIGG ET AL. 14 of 22

measurements by SASSIE at 20-min intervals. For a more meaningful comparison, the shipboard flux time series (thin red line) that were smoothed with a 12-hr running mean (thick red line) was used in the comparison with satellite fluxes (thick black line). Second, satellite retrievals near land and ice edges are susceptible to signal contaminations, rendering them unreliable within 25 km of ice margins or land. Before September 20, the SASSIE vessel frequently operated within or near the marginal ice zone. As a result, satellite data were limited for some time during this period.

The satellite fluxes agree well with the shipboard flux estimates, with some exceptions, particularly for Q_{LW} (Figures 9a–9f). Correlation coefficients between satellite and ship pairs range from 0.73 for Q_{LH} and 0.71 for Q_{SH} to 0.87 for Q_{SW} , but the correlation for Q_{LW} is rather low, at 0.41. It is noted that Q_{LH} , Q_{SH} , and Q_{LW} had reduced correlation before September 20, during the SASSIE vessel's passage through or near the marginal ice zone, where ice contamination affected satellite-based fluxes. While lacking diurnal variations, satellite fluxes align well with the 12-hr smoothed shipboard flux estimates, especially after September 20. The consistency in Q_{LH} between satellite and ship suggests that the 89% RH used in shipboard Q_{LH} estimation is reasonable. For Q_{NET} and τ , the satellite-ship correlations are 0.81 and 0.93, respectively, demonstrating strong agreement in net SEB and winds between the two independent flux estimation approaches.

4.2. Role of Cold Air Outbreaks

The agreement between satellite and shipboard measurements along the ship route (Figure 9) validates the reliability of satellite-derived flux analysis in depicting the basin-wide air-sea conditions in the Beaufort-Chukchi seas during seasonal transition. As shown in Figures 7–9, there was a significant increase in turbulent heat flux following the Autumnal equinox, characterized by intense cold synoptic events, along with changes in wind direction. Two notable synoptic events occurred around September 26 and September 30, during which the total turbulent heat loss exceeded 100 Wm⁻². Figure 10 shows the corresponding spatial distribution of surface winds, air-sea temperature differences $(T_a - T_s)$, and turbulent heat fluxes for these days. For context, it also includes conditions prior to the equinox, represented by the mean average during September 11–20, to provides a comparative baseline.

During September 11–20 (Figures 10a and 10d), conditions across the Beaufort-Chukchi seas were generally mild. The near-surface air temperature, T_a , was marginally higher than SST, T_s , though in some localized areas T_a dipped below T_s . Turbulent heat fluxes were relatively weak, staying within $\pm 20 \, \mathrm{Wm}^{-2}$, and the prevailing winds were easterly. During this time, the SASSIE vessel was navigating near the Beaufort Sea's ice edge, encountering conditions largely in line with the broader basin.

On September 26 (Figures 10b and 10e), there was a significant shift in the patterns of air-sea temperature differences and turbulent heat fluxes. The entire basin experienced colder air, with winds predominately northeasterly. The Chukchi Sea area, west of the Alaska North Slope (Figure 1), was the site of the most intense turbulent heat exchange. Here, $T_a - T_s$ dropped below -4° C and turbulent heat loss exceeded 160 Wm⁻². This event was likely connected to cold mesoscale surface winds emanating from cooling landmasses over Alaska or ice caps in the North Pole toward the warmer seas, a phenomenon presumably driven by the differential cooling rates between the land/ice and ocean due to the waning solar radiation (Zhang et al., 2016). It can be seen that SASSIE vessel experienced these effects, albeit less intensely, as it was positioned north of the main impact zone of this continental cold air.

Four days later, on September 30 (Figures 10c and 10f), the basin continued under the sway of cold air. A significant shift occurred in surface winds, which turned predominantly southward across the central basin. These winds from the North, extending from the ice edge zone near 75°N down to the south of the Chukchi Sea, was associated with large $T_a - T_s$ values, often exceeding -4°C in certain areas. This intense thermal gradient led to intensified oceanic heat loss along the corridor dominated by the winds from the North. The SASSIE vessel, positioned on the eastern fringe of this primary cold air impact zone, experienced the effects of this shift, with turbulent heat fluxes increasing to around -120 Wm^{-2} during this interval (Figure 3).

The satellite flux analysis offered a comprehensive basin-wide perspective that complemented the linewise shipboard measurements, revealing the shifts in air-sea conditions before and after the Autumnal equinox. The marked change in near-surface air temperature, transitioning from slightly warmer than SST to considerably colder, was linked to cold air outbreaks from either Alaska or the perennial sea ice cover near the North Pole. The

CARRIGG ET AL. 15 of 22

21699291, 2024, 5, Downloaded from https://agupubs.onlinelibrary.wikey.com/doi/10.1029/2023J.C020788 by Mbl Whoi Library. Wiley Online Library on [1804/2025]. See the Terms

ditions) on Wiley Online Library for rules

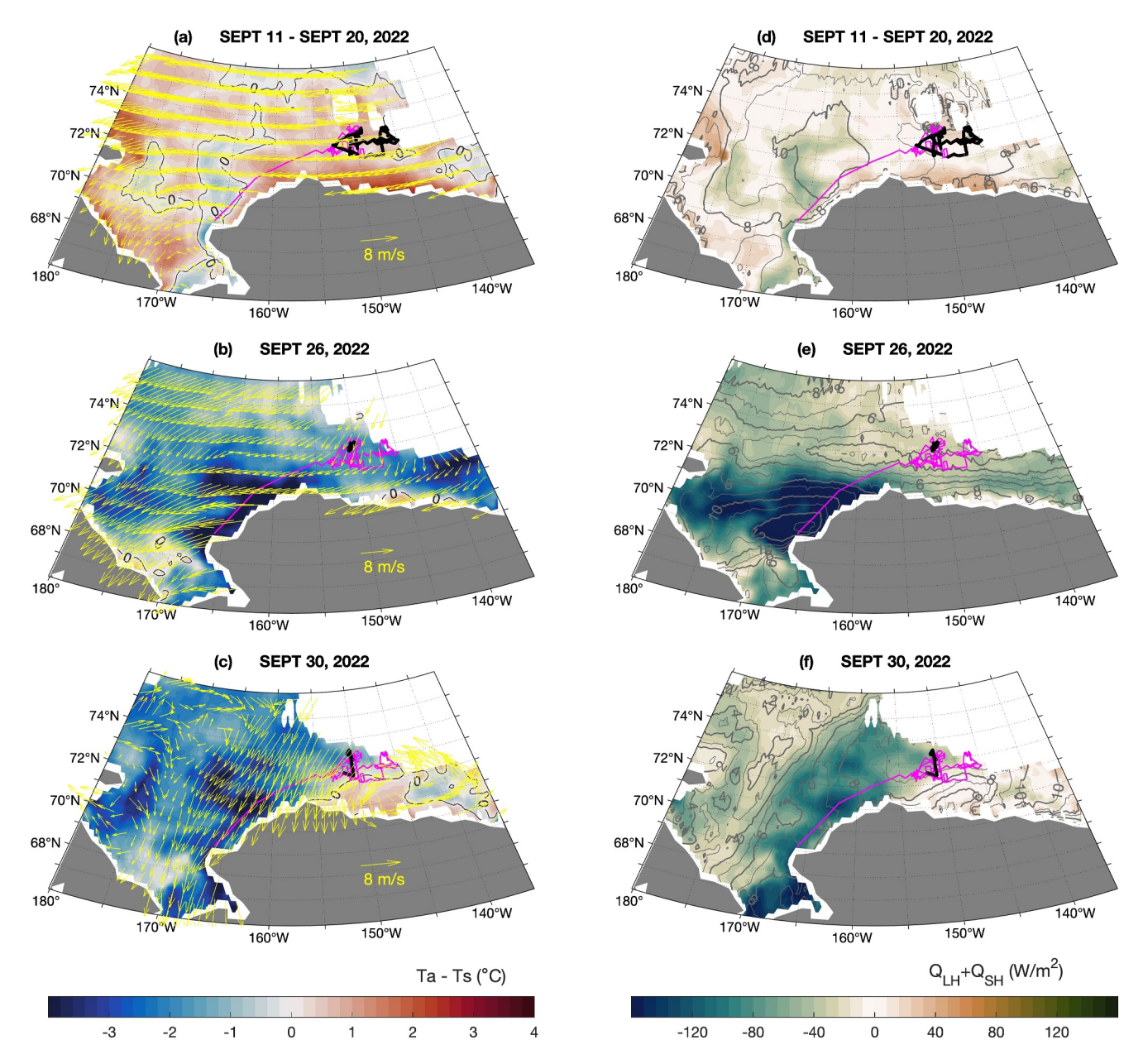


Figure 10. Air-sea variables and fluxes in the Beaufort and Chukchi Seas area for the selected dates during the Salinity and Stratification at the Sea Ice Edge (SASSIE) observation period. Data are from OAFlux2. Left panels (a–c): air-sea temperature difference (Ta - Ts) with surface wind vectors superimposed for the periods 11-20 September, 26 September, and 30 September, 2022, respectively. Right panels (d–f): turbulent heat fluxes $(Q_{LH} + Q_{SH})$ with wind speed contours superimposed for the same time frames. The SASSIE ship route is marked in magenta in all panels, with the section relevant to each panel's time period highlighted in black.

SASSIE vessel captured the essence of this transition in air-sea conditions. However, its position on the fringe of the primary impact zone during these cold air intrusions meant it experienced these changes with less intensity.

4.3. Shifts in Surface Heat Fluxes at the Equinox

To enhance our understanding of the surface energy transition beyond the month-long, route-specific observations, we extended our analysis to the Beaufort-Chukchi seas region from May to December 2022, using satellite flux products. There were barely any ice-free ocean grids in the study domain from January to April 2022, hence this period was not considered. A broader perspective is presented in Figures 11a–11c, which shows daily variations in basin-averaged net surface radiation $(Q_{SW}-Q_{LW})$, total turbulent heat fluxes $(Q_{LH}+Q_{SH})$, and the resultant net surface heat budget (Q_{NET}) over the 8-month period.

CARRIGG ET AL. 16 of 22

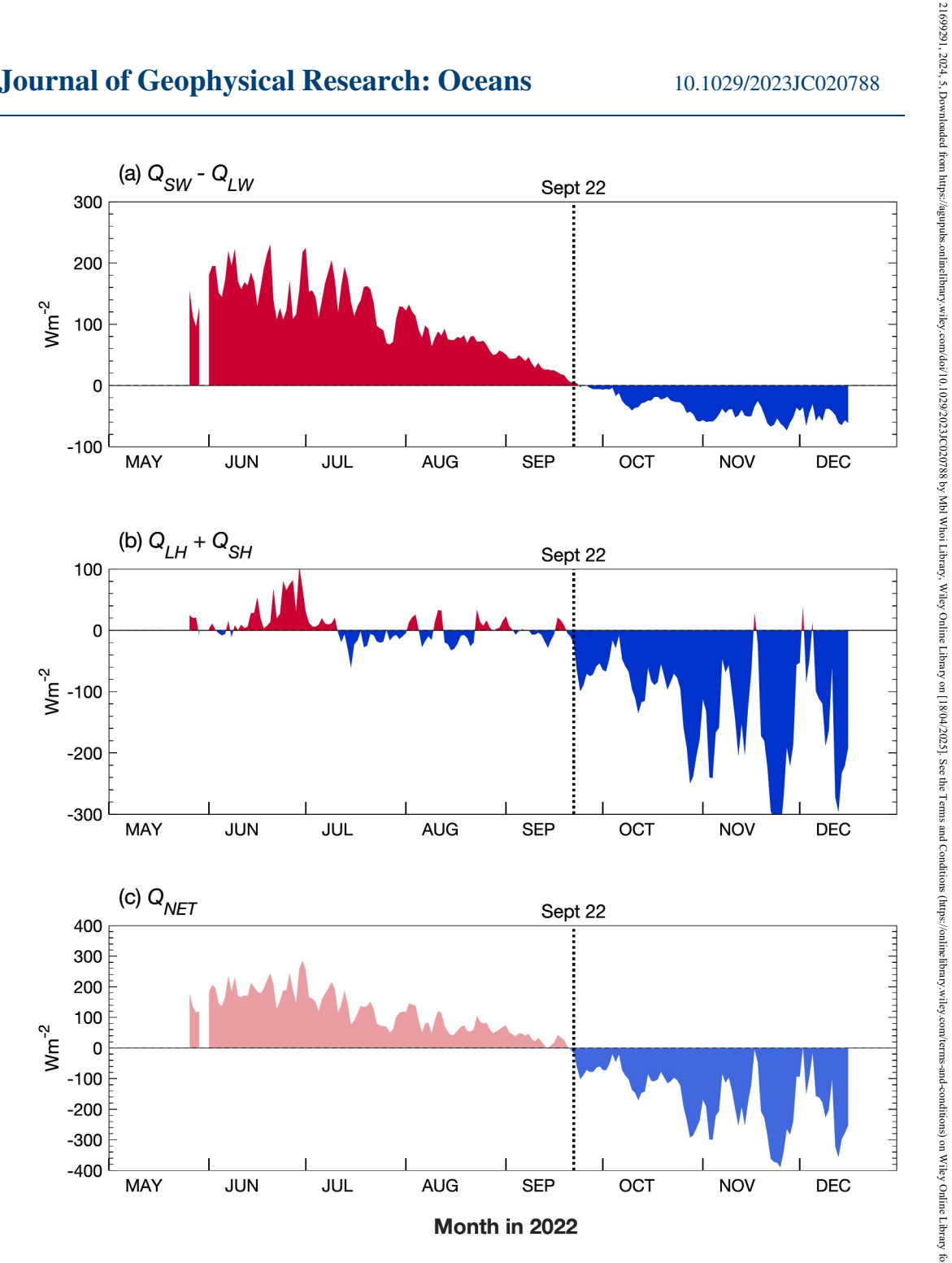


Figure 11. Changes in surface heat fluxes from May to December 2022 averaged over the Beaufort-Chukchi seas area from satellite flux products of CERES and OAFlux2. (a) Net surface radiation, (b) total turbulent heat flux. (c) Net heat flux, Positive values (in red) indicate heat gain by the ocean, while negative values (in blue) denote heat loss from the ocean to the atmosphere. The vertical dashed lines correspond to pivotal changes in surface heat flux patterns, coinciding with the Autumnal equinox.

During this 8-month timeframe, the Beaufort and Chukchi seas region experienced a marked shift in surface radiation (Figure 11a). Sustained net radiative heating dictated the period from late May continuing through late September, peaking during the Arctic summer months of June and July. The maximum intensity exceeded 200 Wm⁻², largely due to the extended daylight of the summer solstice. However, as daylight hours progressively shortened after the solstice, there was a decrease in downward shortwave radiation and in increase in outgoing longwave radiation. This led to a shift in net surface radiation, transitioning from radiative heating to radiative cooling around September 22, aligning with the equinox.

CARRIGG ET AL. 17 of 22 The turbulent heat fluxes (Figure 11b) also underwent a significant transition around the Autumnal equinox, displaying a pattern different from that of surface radiation. Prior to the equinox, turbulent heat exchange remained relatively subdued, featuring a mix of small positive and small negative fluxes. However, immediately after the equinox, turbulent heat fluxes substantially intensified. This increase indicated a more pronounced release of radiative heat, previously absorbed by the ocean, back into the atmosphere. This period coincided with a surge of cold dry air outbreaks, as discussed in Section 4.2, contributing to intensified sea-to-air turbulent heat transfer.

The interplay between radiative and turbulent heat exchanges reached a critical moment around the equinox (Figure 11c). The pattern of heat gain at the ocean surface before this date shifted to a regime of heat loss afterward, as evidenced by the Q_{NET} values changing from positive to negative. This marked a critical turning point in the seasonal energy cycle, indicating that after the equinox, the ocean entered a state of sustained heat loss, releasing more heat to the atmosphere than it absorbed.

4.4. Astronomical Seasons and Surface Heat Energy Transition

The connection between the shifts in Arctic SEB and astronomical seasons is further explored here. The cumulative heat energy is used as a metric to quantify the total energy accumulated or exchanged over the open Beaufort-Chukchi seas. By expanding on the methodology outlined in Equation 6, the cumulative heat energy, E, across the basin is calculated as follows:

$$E = \int Q \, dx \, dy dt \tag{9}$$

This approach differs from Equation 6 that calculates cumulative heat energy along the ship route over a 26-day observing period. Equation 9 extends the integration daily across the entire basin from May to December 2022. E is measured in Zetta Joules (ZJ, 10^{21} J). The integration in Equation 9 is applied to three sets of fluxes, $Q_{SW} - Q_{LW}$, $Q_{LH} + Q_{SH}$, and Q_{NET} , which are denoted as E_{RAD} (radiative energy), E_{TUR} (turbulent energy), and E_{NET} (SEB), respectively.

To elucidate the connection, Figure 12a provides a schematic that shows the Earth's axial tilt and its relationship to the Sun during the four astronomical seasons in year 2022. The diagram illustrates the Earth's tilt at approximately 23.5°, and how this tilt influences the angle of the Sun's rays impinging upon Earth. This axial inclination affects daylight duration and the amount of incoming solar radiation reaching the Arctic Circle (66.6°N), with a peak during the summer solstice on 21 June 2022.

In Figure 12b, the build-up of radiative energy, shown as E_{RAD} (in red), began to increase markedly from the summer solstice, characterized by almost 24 hr of daylight. This increase continued until it reached a peak of approximately 0.15 ZJ on September 22, aligning with the autumnal equinox. The autumnal equinox signaled the start of a steep decline in both daylight hours and solar radiation. Following this date, there was a significant shift: the accumulation of radiative heat began to decrease, and turbulent heat loss, which had been nearly zero before the equinox, started to intensify steadily. This transition is virtually captured by the downward trend of E_{RAD} (in red) and the sharp upward movement of E_{TUR} (in blue). The dynamic shifts in the Arctic heat exchange processes, as the seasons transitions following the equinox, are clearly demonstrated.

The interplay of radiative heat gain and turbulent heat loss, synchronized with the progression of astronomical seasons, culminated in a pronounced peak in the SEB, E_{NET} , at the Autumnal equinox (Figure 12c). This peak represented a critical turning point, shifting from a period of heat accumulation to a period of heat release. By the end of October, the positive phase of E_{NET} had transitioned to a negative phase. As November concluded, both E_{RAD} and E_{TUR} had leveled off, with E_{RAD} reaching approximately 0.1 ZJ and E_{TUR} nearing -0.2 ZJ. At this stage, the Beaufort-Chukchi seas were completely frozen, leaving no ice-free ocean grids.

Evidently, the basin experienced 3 months of heat accumulation from the summer solstice to the autumnal equinox, followed by over 2 months of heat release from late September to late November. It is worth noting that the turbulent heat losses exceeded longwave radiative losses by more than fivefold, collectively driving an intensified heat transfer from the ocean to the atmosphere in the subsequent 2 months, leading to the complete freeze-up of the Beaufort-Chukchi seas by late November. The SASSIE observation period, indicated by light

CARRIGG ET AL. 18 of 22



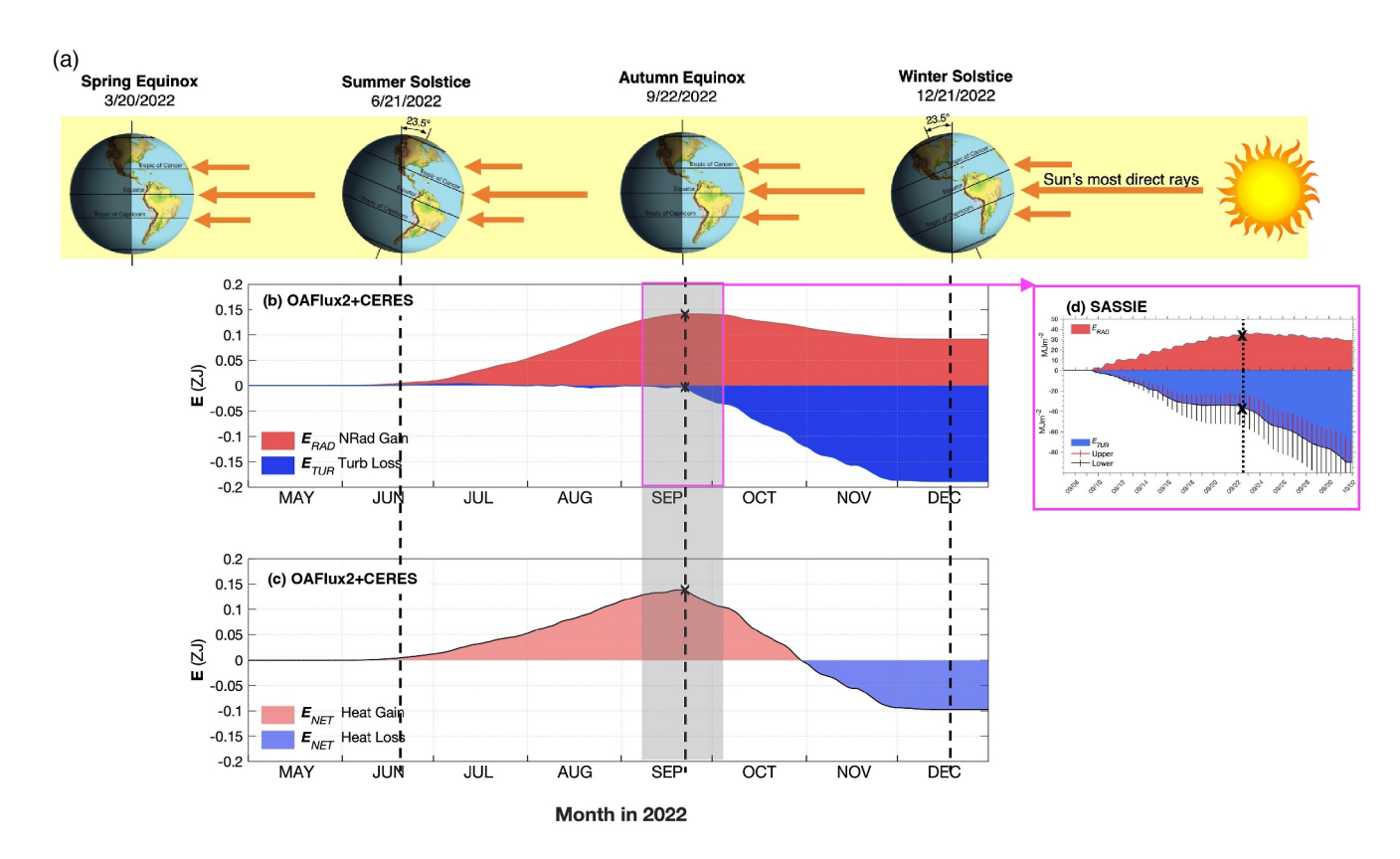


Figure 12. (a) Schematic representation of the Earth's axial tilt and its relation to the Sun over the course of the four astronomical seasons, with the start dates shown for the Northern Hemisphere in 2022. The Earth's axial tilt at about 23.5° regulates the angle at which solar rays strike the Earth's surface and the consequent duration of daylight in the Arctic Circle (66.6°N). Panels (b) and (c) shows the change in heat energy transfers, expressed in Zetta Joules, from May to December 2022 integrated over the Beaufort-Chukchi seas area. In panel (b), net radiative heat energy (E_{RAD}) is indicated by red shading, while turbulent heat energy (E_{TUR}) is shown in blue shading. Panel (c) shows net heat energy (E_{NET}). Positive values of E (in red) indicate a net gain of heat by the ocean surface, while negative values (in blue) denote a net heat loss from the ocean to the atmosphere. In both panels (b) and (c), black "x" symbols, highlight that the key moments in heat energy transfers that align with the Autumn Equinox. These specific moments include the peaks in E_{RAD} and E_{NET} , as well as the onset of significant turbulent heat fluxes (E_{TUR}). Vertical dashed black lines mark the start of the astronomical seasons, including Summer Solstice, Autumnal Equinox, and Winter Solstice. The Salinity and Stratification at the Sea Ice Edge (SASSIE) observation period is shaded in light gray. A magenta box encloses an inset graph in panel (d), depicting the variations in E_{RAD} and E_{NET} along the SASSIE route. These shipboard observed energy shifts align with the broader seasonal heat exchange patterns of the Beaufort-Chukchi seas area as depicted in panels (b) and (c).

gray shading in Figures 12a–12c, corresponds to a crucial energy transition in September. The month-long observations effectively captured the dynamic interplay between surface radiative and turbulent heat energy during this transition period and the shift at the Autumnal equinox (Figure 12d). These shipboard measurements are consistent with satellite flux analysis, emphasizing the profound influence of astronomical seasons on the Arctic SEB and, by implication, on the seasonal pattern of sea ice melting and freezing.

5. Summary

This study investigates the annual cycle of the SEB in the Arctic Ocean, with a particular emphasis on its autumn transition within the Beaufort-Chukchi seas. The analysis draws upon two primary sources of data: high-frequency shipboard measurements collected during the SASSIE experiment from 8 September to 2 October 2022, and daily satellite-based analyses of surface radiation and turbulent heat fluxes throughout 2022. The satellite data supplement the shipboard measurements, offering a more comprehensive spatial and temporal perspective. Three key findings emerged from this analysis, summarized as follows.

The most striking finding is the precise concurrence of the autumnal transition of the SEB with the September 22 equinox. This pivotal astronomical event marks the start of diminishing daylight and a decrease in incoming solar radiation in the Arctic. The shipboard measurements, taken at 20-min intervals, recorded this gradual decline in solar radiation. The data showed a steady drop in daily peak intensity, decreasing at a rate of nearly 11 Wm⁻² per day, from about 400 Wm⁻² to approximately 100 Wm⁻² over the 26-day observation period. This change

CARRIGG ET AL. 19 of 22

indicates a pivotal shift in the SEB, from being primarily influenced by diurnal variations in solar radiation to being dominated by heat loss processes as the season progressed.

The analysis further reveals that the transition in the SEB from heat gain to heat loss at the equinox was not solely due to the increase in outgoing longwave radiation. It also involved a marked rise in turbulent latent and sensible heat losses, coinciding with a surge in synoptic (1–3 days) cold air outbreaks. Satellite data suggest that these outbreaks were likely influenced by cold mesoscale surface winds from cooling landmasses or ice caps moving toward warmer seas. These winds are thought to result from differential cooling rates between land/ice and ocean as solar radiation decreased. Shipboard measurements noted a change in wind direction from predominantly easterly to northeasterly. However, the SASSIE vessel was located at the fringe of the primary impact zone for these events. It effectively captured the essence of these changes in air-sea conditions, albeit with less intensity.

Satellite and shipboard data also showed turbulent heat losses exceeding longwave radiative losses by more than fivefold. This greatly accelerated the heat transfer from the ocean to the atmosphere in the subsequent months, leading to the complete freezing of the Beaufort-Chukchi seas by late November. This finding highlights the significant role of turbulent heat losses in the SEB's autumnal transition possibly more significant than previously acknowledged.

Finally, this study underscores the critical role of turbulent heat loss from the ocean in initiating the sea ice refreezing process during the late summer and early fall, confirming insights from previous studies (Inoue & Hori, 2011; Overland et al., 1996; Taylor et al., 2018; Tietsche et al., 2011). The rapid transfer of accumulated summer heat back to the atmosphere indicates a critical transition phase, during which the Arctic system reconfigures its energy budget to adapt to the diminishing solar heating and the cooler atmospheric conditions. The mechanisms related to oceanic heat release become a key component of this adjustment process. Consequently, these turbulent heat fluxes not only significantly influence the Arctic climate but also hold implications for sea ice dynamics, the dynamics of the marine boundary layer, and the overarching patterns of atmospheric temperature.

Overarching patterns of atmospheric temperature prompt us to consider the broader atmospheric dynamics, particularly the potential influence of large-scale circulation patterns, such as atmospheric blocking (Yao et al., 2024), on the autumnal transition of the SEB. Singular anomalous events like atmospheric blocking may momentarily perturb Q_{NET} , but their overall impact on the seasonal accumulation of heat energy, E, across the Beaufort-Chukchi seas from summer to fall is generally minimal. This minor impact is attributed to the system's ability to absorb and adjust to these transient deviations, thereby maintaining a dynamic equilibrium. However, should atmospheric blocking or similar phenomena persist, they represent a continuous anomaly rather than an isolated event, potentially leading to significant shifts in the heat budget. This enduring pattern has the potential to systematically alter the mean state of E, influencing both its variance and the overall transition of the surface heat budget. The difference between transient anomalies and enduring atmospheric conditions highlights the intricate balance within the Arctic climate system, raising questions about its vulnerability and adaptive capacity in the face of sustained climatic shifts. The implications of these longer-term shifts underscore the necessity for further investigation.

Data Availability Statement

The SASSIE Arctic Field Campaign Shipboard Meteorology Data Fall 2022 (Menezes & Zippel, 2023) are available online (https://doi.org/10.5067/SASSIE-MET2). The documentation for the CERES EBAF surface radiation data set can be found in Loeb et al. (2018) and Kato et al. (2018) and the data are available for download at https://ceres.larc.nasa.gov/data/. The OAFlux data sets are described in Yu and Weller (2007) and Yu (2019) and are available online at https://scienceweb.whoi.edu/oaflux/.

References

Adams, J. M., Bond, N. A., & Overland, J. E. (2000). Regional variability of the Arctic heat budget in fall and winter. *Journal of Climate*, 13(19), 3500–3510. https://doi.org/10.1175/1520-0442(2000)013<3500:RVOTAH>2.0.CO;2

Andreas, E. L., Guest, P. S., Persson, P. O. G., Fairall, C. W., Horst, T. W., Semmer, S. R., & Moritz, R. E. (2002). Near-surface water vapor over polar sea ice is always near ice saturation. *Journal of Geophysical Research*, 107(C10), SHE8-1–SHE8-15. https://doi.org/10.1029/2000JC000411

Bromwich, D., Kuo, Y.-H., Serreze, M., Walsh, J., Bai, L.-S., Barlage, M., et al. (2010). Arctic system reanalysis: Call for community involvement. *Eos, Transactions American Geophysical Union*, 91(2), 13–14. https://doi.org/10.1029/2010E0020001

Acknowledgments

JC would like to acknowledge the WHOI Summer Student Fellowship for its support of this summer research project. LY extends sincere thanks to the NOAA Climate Program Office (Grant NA20OAR4310370) and the NASA Ocean Vector Wind Science Team (OVWST) program (Grant 80NSSC23K0981) for funding support related to Arctic surface fluxes and winds research, Additionally, LY acknowledges the NASA Making Earth System Data Records for Use in Research Environments (MEaSUREs) program (Grant 80NSSC18M0079) and the NOAA Ocean Monitoring and Observing (GOMO) program (Grant NA19OAR4320074) for funding support to the development of OAFlux2 flux products. VVM was supported by the NASA SASSIE project (Grant 80NSSC21K0832). The authors extend their gratitude to the individuals who made this study possible: the R/V Woldstad crew and the SASSIE fieldwork team-Kyla Drushka, Jim Thomson, Peter Gaube, Julian Schanze, Justin Burnett, Jaynise Pérez, Carlyn Schmidgall, Léa Olivier, Laetitia Parc, EJ Rainville, and VVM. Special thanks to WHOI Engineers Stephen Faluotico and John Sisson for setting up the shipboard surface meteorological data collection system and providing real-time land support. We also thank Seth Zippel for providing the SASSIE flux data sets, Liz Westbrook for making SASSIE data easily accessible to the broad community, and Mike Steel for discussions on our research findings.

CARRIGG ET AL. 20 of 22



Journal of Geophysical Research: Oceans

- 10.1029/2023JC020788
- Businger, S. (1987). The synoptic climatology of polar-low outbreaks over the Gulf of Alaska and the Bering Sea. *Tellus A: Dynamic Meteorology and Oceanography*, 39(4), 307–325. https://doi.org/10.1111/j.1600-0870.1987.tb00310.x
- Cayan, D. R. (1992). Variability of latent and sensible heat fluxes estimated using bulk formulae. Atmosphere-Ocean, 30, 1–42. https://doi.org/10.1080/07055900.1992.9649429
- Cohen, L., Hudson, S. R., Walden, V. P., Graham, R. M., & Granskog, M. A. (2017). Meteorological conditions in a thinner Arctic sea ice regime from winter to summer during the Norwegian Young Sea ice expedition (N-ICE2015). *Journal of Geophysical Research: Atmospheres*, 122(14), 7235–7259. https://doi.org/10.1002/2016JD026034
- Comiso, J. C., Parkinson, C. L., Gersten, R., & Stock, L. (2008). Accelerated decline in the Arctic sea ice cover. *Geophysical Research Letters*, 35(1), L01703. https://doi.org/10.1029/2007GL031972
- Cox, C. J., Gallagher, M. R., Shupe, M. D., Persson, P. O. G., Solomon, A., Fairall, C. W., et al. (2023). Continuous observations of the surface energy budget and meteorology over the Arctic sea ice during MOSAiC. *Scientific Data*, 10(1), 519. https://doi.org/10.1038/s41597-023-02415-5
- Cullather, R. I., & Bosilovich, M. G. (2012). The energy budget of the polar atmosphere in MERRA. *Journal of Climate*, 25(1), 5–24. https://doi.org/10.1175/2011JCLI4138.1
- Doelling, D. R., Loeb, N. G., Keyes, D. F., Nordeen, M. L., Morstad, D., Nguyen, C., et al. (2013). Geostationary enhanced temporal interpolation for CERES flux products. *Journal of Atmospheric and Oceanic Technology*, 30(6), 1072–1090. https://doi.org/10.1175/JTECH-D-12-00136.1
- Drushka, K., Westbrook, E., Bingham, F., Gaube, P., Dickinson, S., Fournier, S., et al. (2024). Salinity and stratification at the sea ice edge (SASSIE): An oceanographic field campaign in the Beaufort Sea. Earth System Science Data Discussions. (preprint), in press. https://doi.org/10.5194/essd-2023-406
- Edson, J. B., Jampana, V., Weller, R. A., Bigorre, S. P., Plueddemann, A. J., Fairall, C. W., et al. (2013). On the exchange of momentum over the open ocean. *Journal of Physical Oceanography*, 43(8), 1589–1610. https://doi.org/10.1175/JPO-D-12-0173.1
- Emanuel, K., & Rotunno, R. (1989). Polar lows as Arctic hurricanes. Tellus, 41A, 1-17. https://doi.org/10.1111/j.1600-0870.1989.tb00362.x
- Fairall, C. W., Bradley, E. F., Hare, J. E., Grachev, A. A., & Edson, J. B. (2003). Bulk parameterization of air-sea fluxes: Updates and verification for the COARE algorithm. *Journal of Climate*, 16(4), 571–591. https://doi.org/10.1175/1520-0442(2003)016<0571:BPOASF>2.0.CO;2
- Fletcher, J., Mason, S., & Jakob, C. (2016). The climatology, meteorology, and boundary layer structure of marine cold air outbreaks in both hemispheres. *Journal of Climate*, 29(6), 1999–2014. https://doi.org/10.1175/jcli-d-15-0268.1
- Fore, I., Kristjansson, J. E., Kolstad, E. W., Bracegirdle, T. J., Saetra, O., & Rosting, B. (2012). A hurricanelike polar low fuelled by sensible heat flux: High-resolution numerical simulations. *Quarterly Journal of the Royal Meteorological Society*, 138(666), 1308–1324. https://doi.org/10. 1002/qj.1876
- Gettelman, A., Walden, V. P., Miloshevich, L. M., Roth, W. L., & Halter, B. (2006). Relative humidity over Antarctica from radiosondes, satellites, and a general circulation model. *Journal of Geophysical Research*, 111(D9), D09S13. https://doi.org/10.1029/2005JD006636
- Inoue, J., & Hori, M. E. (2011). Arctic cyclogenesis at the marginal ice zone: A contributory mechanism for the temperature amplification. Geophysical Research Letters, 38(12), L12502. https://doi.org/10.1029/2011GL047696
- Kato, S., Rose, F. G., Rutan, D. A., Thorsen, T. J., Loeb, N. G., Doelling, D. R., et al. (2018). Surface irradiances of edition 4.0 clouds and the Earth's radiant energy system (CERES) energy balanced and filled (EBAF) data product. *Journal of Climate*, 31(11), 4501–4527. https://doi. org/10.1175/JCL1-D-17-0523.1
- Kozo, T. (1980). Mountain barrier baroclinity effects on surface winds along the Alaskan Arctic coast. Geophysical Research Letters, 7(5), 377–380. https://doi.org/10.1029/gl007i005p00377
- Liu, A. Q., Moore, G. W. K., Tsuboki, K., & Renfrew, I. A. (2004). A high-resolution simulation of convective roll clouds during a cold-air outbreak. Geophysical Research Letters, 31(3), L03101. https://doi.org/10.1029/2003GL018530
- Loeb, N. G., Doelling, D. R., Wang, H., Su, W., Nguyen, C., Corbett, J. G., et al. (2018). Clouds and the Earth's radiant energy system (CERES) energy balanced and filled (EBAF) top-of-atmosphere (TOA) edition-4.0 data product. *Journal of Climate*, 31(2), 895–918. https://doi.org/10.1175/JCLI-D-17-0208.1
- Lynch, A. H., Curry, J. A., Brunner, R. D., & Maslanki, J. A. (2004). Toward an integrated assessment of the impacts of extreme wind events on Barrow, Alaska. *Bulletin of the American Meteorological Society*, 209–221.
- Mayer, M., Haimberger, L., Pietschnig, M., & Storto, A. (2016). Facets of Arctic energy accumulation based on observations and reanalyses 2000–2015. Geophysical Research Letters, 43(19), 10420–10429. https://doi.org/10.1002/2016GL070557
- Menezes, V., & Zippel, S. (2023). SASSIE Arctic field campaign shipboard meteorology data fall 2022. Ver. 1 [Dataset]. PO.DAAC. https://doi.org/10.5067/SASSIE-MET2
- Nakamura, N., & Oort, A. H. (1988). Atmospheric heat budgets of the polar regions. *Journal of Geophysical Research*, 93(D8), 9510–9524. https://doi.org/10.1029/JD093iD08p09510
- Onarheim, I. H., Eldevik, T., Smedsrud, L. H., & Stroeve, J. C. (2018). Seasonal and regional manifestation of Arctic sea ice loss. *Journal of Climate*, 31(12), 4917–4932. https://doi.org/10.1175/JCLI-D-17-0427.1
- Overland, J., Dunlea, E., Box, J. E., Corell, R., Forsius, M., Kattsov, V., et al. (2019). The urgency of Arctic change. *Polar Science*, 21, 6–13. https://doi.org/10.1016/j.polar.2018.11.008
- Overland, J. E. (2009). Meteorology of the Beaufort Sea. *Journal of Geophysical Research*, 114(C1), C00A07. https://doi.org/10.1029/2008JC004861
- Overland, J. E., & Turet, P. (1994). Variability of the atmospheric energy flux across 70°N computed from the GFDL data set. In R. D. Muench, & J. E. Overland (Eds.), *The polar oceans and their role in shaping the global environment, the Nansen centennial volume, Geophysical Monograph* (Vol. 85, pp. 313–325). AGU.
- Overland, J. E., Turet, P., & Oort, A. H. (1996). Regional variation of moist static energy flux into the Arctic. *Journal of Climate*, 9(1), 54–65. https://doi.org/10.1175/1520-0442(1996)009<0054:RVOMSE>2.0.CO;2
- Perovich, D. K., Andreas, E. L., Curry, J. A., Eiken, H., Fairall, C. W., Grenfell, T. C., et al. (1999). Year on ice gives climate insights. *Eos, Transactions American Geophysical Union*, 80(41), 481–486. https://doi.org/10.1029/EO080i041p00481-01
- Perovich, D. K., & Polashenski, C. (2012). Albedo evolution of seasonal Arctic sea ice. Geophysical Research Letters, 39(8), L08501. https://doi.org/10.1029/2012GL051432
- Pichugin, M. K., Gurvich, I. A., & Zabolotskikh, E. V. (2019). Severe marine weather systems during freeze-up in the Chukchi Sea: Cold-air outbreak and mesocyclone case studies from satellite multisensor measurements and reanalysis datasets. IEEE Journal of Selected Topics in Applied Earth Observations and Remote Sensing, 12(9), 3208–3218. https://doi.org/10.1109/jstars.2019.2934749
- Porter, D. F., Cassano, J. J., Serreze, M. C., & Kindig, D. N. (2010). New estimates of the large-scale Arctic atmospheric energy budget. *Journal of Geophysical Research*, 115(D8), D08108. https://doi.org/10.1029/2009JD012653
- Przybylak, R. (2016). The climate of the Arctic (2nd ed., p. 287). Springer

CARRIGG ET AL. 21 of 22

- Rantanen, M., Karpechko, A. Y., Lipponen, A., Nordling, K., Hyvärinen, O., Ruosteenoja, K., et al. (2022). The Arctic has warmed nearly four times faster than the globe since 1979. Communications Earth & Environment, 3(1), 168. https://doi.org/10.1038/s43247-022-00498-3
- Ricker, R., Kauker, F., Schweiger, A., Hendricks, S., Zhang, J., & Paul, S. (2021). Evidence for an increasing role of ocean heat in Arctic winter sea ice growth. *Journal of Climate*, 34, 5215–5227. https://doi.org/10.1175/JCLI-D-20-0848.1
- Semmler, T., McGrath, R., & Wang, S. (2012). The impact of Arctic sea ice on the Arctic energy budget and on the climate of the Northern mid-latitudes. Climate Dynamics, 39(11), 2675–2694. https://doi.org/10.1007/s00382-012-1353-9
- Serreze, M. C., Barrett, A. P., Slater, A. G., Steele, M., Zhang, J., & Trenberth, K. E. (2007). The large-scale energy budget of the Arctic. *Journal of Geophysical Research*, 112(D11), D11122. https://doi.org/10.1029/2006JD008230
- Serreze, M. C., & Barry, R. G. (2011). Processes and impacts of Arctic amplification: A research synthesis. *Global and Planetary Change*, 77(1–2), 85–96. https://doi.org/10.1016/j.gloplacha.2011.03.004
- Shepard, D. (1968). A two-dimensional interpolation function for irregularly-spaced data. In *Proceedings of the 1968 23rd ACM national conference (ACM '68)* (Vol. 23, pp. 517–524), https://doi.org/10.1145/800186.81061
- Shupe, M. D., Rex, M., Blomquist, B., Persson, P. O. G., Schmale, J., Uttal, T., et al. (2022). Overview of the MOSAiC expedition: Atmosphere. Elementa: Science of the Anthropocene, 10(1), 00060. https://doi.org/10.1525/elementa.2021.00060
- Steele, M., & Dickinson, S. (2016). The phenology of Arctic Ocean surface warming. *Journal of Geophysical Research: Oceans*, 121(9), 6847–6861. https://doi.org/10.1002/2016JC012089
- Stegall, S. T., & Zhang, J. (2012). Wind field climatology, changes, and extremes in the Chukchi–Beaufort seas and Alaska North Slope during 1979–2009. *Journal of Climate*, 25(23), 8075–8089. https://doi.org/10.1175/JCLI-D-11-00532.1
- Stoll, P. J., Graversen, R. G., Noer, G., & Hodges, K. (2018). An objective global climatology of polar lows based on reanalysis data. *Quarterly Journal of the Royal Meteorological Society*, 144(716), 2099–2117. https://doi.org/10.1002/qj.3309
- Stroeve, J. C., Markus, T., Boisvert, L., Miller, J., & Barrett, A. (2014). Changes in Arctic melt season and implications for sea ice loss. Geophysical Research Letters, 41(4), 1216–1225. https://doi.org/10.1002/2013GL058951
- Stroeve, J. C., Serreze, M. C., Holland, M. M., Kay, J. E., Malanik, J., & Barrett, A. P. (2012). The Arctic's rapidly shrinking sea ice cover: A
- research synthesis. Climatic Change, 110(3–4), 1005–1027. https://doi.org/10.1007/s10584-011-0101-1
 Taylor, P. C., Hegyi, B. M., Boeke, R. C., & Boisvert, L. N. (2018). On the increasing importance of air-sea exchanges in a Thawing Arctic: A review. Atmosphere, 9(2), 41. https://doi.org/10.3390/atmos9020041
- Tietsche, S., Notz, D., Jungclaus, J. H., & Marotzke, J. (2011). Recovery mechanisms of Arctic summer sea ice. *Geophysical Research Letters*, 38(2), L02–L707. https://doi.org/10.1029/2010GL045698
- Timmermans, M. L. (2015). The impact of stored solar heat on Arctic sea ice growth. Geophysical Research Letters, 42(15), 6399–6406. https://doi.org/10.1002/2015GL064541
- doi.org/10.1002/2015GL064541
 Trenberth, K., Caron, J., & Stepaniak, D. (2001). The atmospheric energy budget and implications for surface fluxes and ocean heat transports.
- Climate Dynamics, 17(4), 259–276. https://doi.org/10.1007/PL00007927
 Tsubouchi, T., Bacon, S., Aksenov, Y., Garabato, A. C. N., Beszczynska-Möller, A., Hansen, E., et al. (2018). The Arctic Ocean seasonal cycles of
- Tsubouchi, T., Bacon, S., Aksenov, Y., Garabato, A. C. N., Beszczynska-Möller, A., Hansen, E., et al. (2018). The Arctic Ocean seasonal cycles of heat and freshwater fluxes: Observation-based inverse estimates. *Journal of Physical Oceanography*, 48(9), 2029–2055. https://doi.org/10.1175/JPO-D-17-0239.1
- UK Met Office. (2005). OSTIA L4 SST analysis. Ver. 1.0 [Dataset]. PO.DAAC. https://doi.org/10.5067/GHOST-4FK01
- Uttal, T., Curry, J. A., Mcphee, M. G., Perovich, D. K., Moritz, R. E., Maslanik, J. A., et al. (2002). Surface heat budget of the Arctic Ocean. Bulletin of the American Meteorological Society, 83(2), 255–275. https://doi.org/10.1175/1520-0477(2002)083<0255:SHBOTA>2.3.CO;2
- Vüllers, J., Achtert, P., Brooks, I. M., Tjernström, M., Prytherch, J., Burzik, A., & Neely, R., III. (2020). Meteorological and cloud conditions during the Arctic Ocean 2018 expedition. Atmospheric Chemistry and Physics, 21(1), 289–314. https://doi.org/10.5194/acp-21-289-2021
- Yao, Y., Zhuo, W. Q., Luo, D. H., Simmonds, I., Luo, B. H., Zhong, L. H., & Huang, F. (2024). Impact of Pacific blocking on the intraseasonal winter sea ice seesaw between the Bering and Okhotsk seas. Atmospheric Research, 300, 107227. https://doi.org/10.1016/j.atmosres.2024. 107227
- Yu, L. (2019). Global air–sea fluxes of heat, fresh water, and momentum: Energy budget closure and unanswered questions. Annual Review of Marine Science, 11(1), 227–248. https://doi.org/10.1146/annurev-marine-010816-060704
- Yu, L. (2021). Emerging pattern of wind change over the Eurasian Marginal seas revealed by three decades of satellite ocean-surface wind observations. Special issue "Remote sensing of air-sea fluxes". Remote Sensing, 13(9), 1707. https://doi.org/10.3390/rs13091707
- Yu, L., Chen, Y., Gonzalez, A. O., Zhang, C., & Foltz, G. R. (2023). Dry air outbreak and significant surface turbulent heat loss during Hurricane Ian: Satellite and saildrone observations. *Geophysical Research Letters*, 50(23), e2023GL105583. https://doi.org/10.1029/2023GL105583
- Yu, L., & Jin, X. (2014). Insights on the OAFlux ocean surface vector wind analysis merged from scatterometers and passive microwave radiometers (1987 onward). *Journal of Geophysical Research: Oceans*, 119(8), 5244–5269. https://doi.org/10.1002/2013JC009648
- Yu, L., & Jin, X. (2018). A regime-dependent retrieval algorithm for near-surface air temperature and specific humidity from multi-microwave sensors. Remote Sensing of Environment, 215, 199–216. https://doi.org/10.1016/j.rse.2018.06.001
- Yu, L., Jin, X., & Schulz, E. W. (2019). Surface heat budget in the Southern Ocean from 42°S to the Antarctic marginal ice zone: Four atmospheric reanalyses versus icebreaker aurora measurements. *Polar Research*, 38(0). https://doi.org/10.33265/polar.v38.3349
- Yu, L., & Weller, R. A. (2007). Objectively analyzed air–sea heat fluxes for the global ice-free oceans (1981–2005). Bulletin America Meteorology Social, 88(4), 527–540. https://doi.org/10.1175/BAMS-88-4-527
- Zhang, J. (2021). Recent slowdown in the decline of Arctic sea ice volume under increasingly warm atmospheric and oceanic conditions. Geophysical Research Letters, 48(18), e2021GL094780. https://doi.org/10.1029/2021GL094780
- Zhang, J., Liu, F., Tao, W., Krieger, J., Shulski, M., & Zhang, X. (2016). Mesoscale climatology and variation of surface winds over the Chukchi–Beaufort coastal areas. *Journal of Climate*, 29(8), 2721–2739. https://doi.org/10.1175/JCLI-D-15-0436.1
- Zhang, J., Stegall, S. T., & Zhang, X. (2018). Wind–sea surface temperature–sea ice relationship in the Chukchi–Beaufort Seas during autumn. Environmental Research Letters, 13(3), 034008. https://doi.org/10.1088/1748-9326/aa9adb

CARRIGG ET AL. 22 of 22